

A Difference-in-Difference Approach to Detecting AI-Generated Images

Xinyi Qi*

Tsinghua University

qixy25@mails.tsinghua.edu.cn

Chengchun Shi

The London School of Economics and Political Science

c.shi7@lse.ac.uk

Hongyi Zhou[†]

Tsinghua University

zhou-hy21@mails.tsinghua.edu.cn

Kai Ye*

The London School of Economics and Political Science

k.ye1@lse.ac.uk

Ying Yang

Tsinghua University

yangying@tsinghua.edu.cn

Jin Zhu[†]

University of Birmingham

j.zhu.7@bham.ac.uk

Abstract

Diffusion models are able to produce AI-generated images that are almost indistinguishable from real ones. This raises concerns about their potential misuse and poses substantial challenges for detecting them. Many existing detectors rely on reconstruction error — the difference between the input image and its reconstructed version — as the basis for distinguishing real from fake images. However, these detectors become less effective as modern AI-generated images become increasingly similar to real ones. To address this challenge, we propose a novel difference-in-difference method. Instead of directly using the reconstruction error (a first-order difference), we compute the difference in reconstruction error — a second-order difference — for variance reduction and improving detection accuracy. Extensive experiments demonstrate that our method achieves strong generalization performance, enabling reliable detection of AI-generated images in the era of generative AI.

1. Introduction

The rapid evolution of large-scale generative models has led to groundbreaking progress in image generation in recent years [2, 4, 6, 9, 69]. Diffusion models, in particular, have become the foundation of modern image generation. However, the proliferation of AI-generated images has raised substantial concerns about authenticity and public trust, cre-

*Xinyi Qi and Kai Ye contributed equally to this work and are listed in alphabetical order.

[†]Corresponding authors: Hongyi Zhou and Jin Zhu are listed in alphabetical order. Emails: zhou-hy21@mails.tsinghua.edu.cn, j.zhu.7@bham.ac.uk

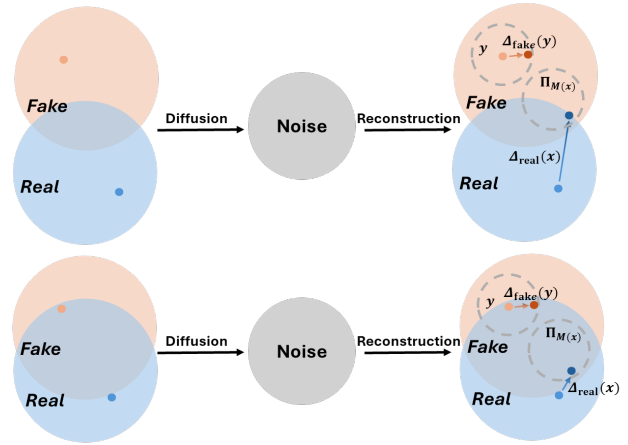


Figure 1. **Left:** The real image x and its distribution on the manifold \mathcal{M} are shown in blue, whereas the synthetic image y and its distribution are shown in orange. **Right:** Reconstructions of the real and synthetic images. Δ_{fake} and Δ_{real} denote the reconstruction errors of synthetic and real images, respectively, and $\Pi_{\mathcal{M}}$ represents the projection of the real image onto \mathcal{M} . **Top:** The generator is weak, resulting in a large discrepancy between the real and synthetic image distributions. Consequently, the reconstruction error of the synthetic image, $\Delta_{\text{fake}}(y)$, is much larger than that of the real image, $\Delta_{\text{real}}(x)$, making detection easier. **Bottom:** The generator is strong, so the real and synthetic image distributions are close. Here, $\Delta_{\text{fake}}(y)$ is similar to $\Delta_{\text{real}}(x)$, making AI-generated images difficult to detect.

ating an urgent need for effective detectors that can distinguish AI-generated images from real ones. There is a growing literature on detecting AI-generated images; see Section 2 for a detailed review. Early detection algorithms were tailored for specific models and exploited model-based arti-

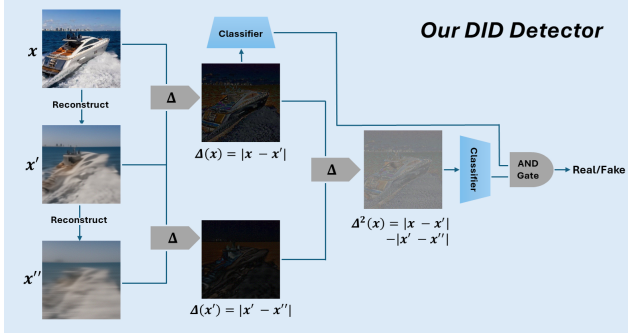


Figure 2. Visualizations of our DID detector. Δ denotes the differencing operator that computes the pixel-wise difference between two images.

facts — such as inconsistencies in the frequency domain, irregularities in color filter responses, or statistical traces introduced by up-sampling layers [21, 28, 95]. Although these methods achieved strong performance in detecting images from specific generators, they lacked robustness across different models.

More recently, reconstruction-based algorithms have emerged as both conceptually intuitive and effective practically. As suggested by their name, these methods (a) reconstruct the image to be detected using a generative model (e.g., a diffusion model), (b) compute the reconstruction error as the difference between the original and reconstructed images, and (c) classify the image as real or synthetic based on that error. Their core idea is straightforward: given a particular generative model for reconstruction, synthetic images that lie on or near the model manifold should be reconstructed with smaller residual errors than real images, which reside outside that manifold (see the upper panel of Figure 1 for an illustration). This line of work, represented by DIRE [80] and its variants LaRE² and FIRE [19, 49], has generalized well across different generative models, while maintaining a transparent interpretation.

However, the effectiveness of existing reconstruction-based algorithms relies on a sufficiently large gap between real and AI-generated images to be detectable. As generative models advance rapidly, this assumption becomes increasingly invalid. Meanwhile, images found on the internet are often post-processed, through resizing, compression, or partial AI editing (where only specific regions are synthesized), which further confounds detection signals. Recent studies have empirically observed that as the quality of the image generator improves or under adversarial scenarios (e.g., with partial AI edits), reconstruction-based algorithms struggle to detect AI-generated content effectively [19, 79]. See also, the bottom panel of Figure 1 for an illustration. Therefore, as high-fidelity diffusion models become prevalent, it is necessary to move beyond existing reconstruction-

based methods and develop more effective algorithms capable of detecting subtler differences between real and AI-generated content.

This paper proposes a new algorithm, termed *difference-in-differences* (DID), for detecting AI-generated content. Instead of relying solely on the reconstruction error — which can be viewed as a *first-order* difference between the input image and its reconstruction — we compute a *second-order* difference by taking the difference between the reconstruction error of the input image and the reconstruction error of its reconstructed version. Our analytical analysis in Section 3 shows that this second-order differencing can effectively remove fluctuations introduced during synthetic image generation, thus amplifying the detection signal particularly when it is weak. We next employ both first-order and second-order differences as the basis for detection (see Figure 2 for an illustration of our proposal). Empirically, our extensive numerical experiments demonstrate that DID consistently outperforms existing detectors across diverse combinations of image datasets and generative models, achieving improvements around 20% - 30% over the strongest baseline. Moreover, our findings shed light on the effectiveness of DID: in simpler settings where AI-generated images are sufficiently different from real ones, first-order differences alone are adequate for detection; however, in more complex experimental settings, employing the second-order difference substantially improves the detection accuracy. These observations are consistent with our analytical insights. By leveraging both orders of differences, our method generalizes robustly across a wide range of detection tasks.

2. Related Works

This section is organized as follows. We begin by reviewing various diffusion models used for image generation. We then review existing algorithms for AI-image detection. Finally, we introduce the difference-in-difference (DID) method from econometrics, which is conceptually related to our proposal but fundamentally different in terms of its problem setting and application.

2.1. Diffusion Models

Diffusion models have become a cornerstone of modern image generation and multimodal large language models [MLLMs, 36, 90], powering a wide range of tasks such as text-to-image, text-to-3D generation, and text-to-video generation [23, 31, 34, 43, 55, 59, 62, 63, 66, 67, 89, 92]. They constitute an important family of probabilistic generative models that progressively perturb data with noise and learn a reverse process to generate synthetic samples [87]. Broadly speaking, these models can be categorized into three main types: denoising diffusion probabilistic models [33, 70], score-based generative models [72, 73], and stochastic differential equation (SDE)-based models

[74, 75]. Building on the three types of models described above, each can be further decomposed into two subtypes: unconditional and conditional diffusion models. For unconditional diffusion models, prior research has focused on three directions: (i) accelerating the sampling process [26, 39, 72, 81, 93, 94], (ii) tightening the variational lower bound on the data log-likelihood [7, 40, 48, 56, 71], and (iii) extending the model to accommodate new data modalities [12, 35, 38, 57, 77]. By contrast, research on conditional diffusion models has focused on guiding the generation process to produce content that aligns with users’ desired specifications. For instance, ADM uses an auxiliary classifier to improve the quality of generated samples [25]. ImageReward [84] and Diffusion-DPO [78] leverage reinforcement learning from human feedback to align diffusion models with human preferences. Scalable diffusion models [60] replace standard layer normalization in transformers with adaptive layer normalization to more effectively encode conditioning variables. DiffuSeq [29], unCLIP [63], ConPreDif [86], and RPG [88] focus on guiding diffusion models with textual inputs.

2.2. AI-Generated Image Detection

With the rapid advancement of AI image generators, there is an urgent need to detect AI-generated images; see [45] for a recent review of detection algorithms.

Early works leverage physical [11, 27, 51, 52] and physiological features [20] in the images, such as inconsistencies in color, perspective, shadows, reflections or human anatomy for detection. These methods rely on the assumption that AI-generated images often fail to adhere to real-world physical and physiological constraints. Later approaches employ spatial-domain features, such as the image texture to build classifiers [47, 54, 96]. However, such classifiers often fail to capture frequency-domain artifacts [82]. To overcome this limitation, several methods have been proposed that combine spatial- and frequency-domain features for detection [5, 41, 82, 83]. Other approaches leverage alternative features, such as the negative log-likelihood of the input image [22], or directly fine-tune an MLLM [44] for detection.

Different from the aforementioned approaches, our proposal is most closely related to reconstruction-based detection algorithms. As discussed in the introduction, a representative example is DIRE [80], which employs a diffusion model with a forward diffusion process and a reverse denoising process to obtain the reconstruction, computes the difference from the original image as the reconstruction error, and trains the classifier using this reconstruction error. SeDID [50] extends this approach by considering not only the final reconstruction error between the reconstructed and input image, but also the intermediate errors accumulated along the forward diffusion and reverse denoising pro-

cesses. Other variants, such as DRCT [17], modify the objective function by employing a contrastive loss to train the classifier based on the reconstruction error. One potential limitation of DIRE is its computational time required to obtain the reconstruction, as the forward diffusion and reverse denoising processes involve multiple steps and can be time-consuming. To address this, LaRE² [49] projects the image into a latent space and applies the forward and reverse procedures only once, computing the reconstruction error in the latent space to speed up the computation. AEROBLADE [64] adopts a training-free strategy: instead of training a classifier with the reconstruction error, it relies on simple statistical measures derived from the reconstruction error for detection. FakeInversion [16] inverts an open-source stable diffusion process model to compute the reconstruction error. Finally, FIRE additionally leverages frequency-domain information to compute reconstruction errors, which enhances the detector’s robustness in adversarial settings and across different generative models [19].

2.3. Difference-in-Differences

Our proposal is conceptually similar to the difference-in-difference approach for causal inference, which estimates the treatment effect of a particular policy. DID originated in social science research on quasi-experimental designs [14, 37] and was later systematized and popularized in the econometrics literature for analyzing panel data with multiple subjects observed over time [3, 10, 15].

In the typical DID setting, some subjects are continuously exposed to a control policy, while others switch from the control to a new policy at a certain time point. For the latter group, one can compute a first-order difference in their average outcomes before and after the policy change. However, this difference captures not only the effect of the policy but also any time-related effects. To remove the confounding effect of time, a corresponding first-order difference is computed for the control group, and a second-order difference between the two first-order differences is then taken to isolate the treatment effect. For more details, refer to [1, 13, 30, 76].

Despite sharing the same name and similar conceptual ideas, our proposal is designed for a fundamentally different application of AI-generated image detection, as opposed to causal inference.

3. Methodology

This section first provides background on diffusion models (Section 3.1), then discusses the intuition and limitations of existing reconstruction-based methods (Section 3.2), which motivates our use of DID (Section 3.3). Finally, we detail our proposal (Section 3.4).

3.1. Background on Diffusion Models

Image generation via diffusion models typically consists of two processes: a *forward diffusion* process that gradually corrupts data with Gaussian noise, and a *reverse denoising* process that reconstructs the underlying image signal from noise. Specifically, in the forward process, an image x_0 is progressively transformed into a sequence of noisy images $\{x_t\}_{t=1}^T$ according to

$$x_t = \sqrt{\alpha_t}x_{t-1} + \sqrt{1 - \alpha_t} \epsilon_t,$$

for $t = 1, \dots, T$, where x_t denotes the noisy image at timestep t , and $\bar{\alpha}_t = \prod_{i=1}^t \alpha_i$ for a sequence of pre-defined weights $\{\alpha_t\}_t$ that controls the signal-to-noise ratio and $\epsilon_t \sim \mathcal{N}(0, I)$ is the Gaussian noise.

In contrast, during the reverse process, the model learns to iteratively denoise x_t back to a clean sample using a parameterized neural network $\epsilon_\theta(x_t, t)$ that takes x_t and t as input and aims to predict the added noise ϵ_t . This process can be mathematically represented by

$$x_{t-1} = \frac{1}{\sqrt{\alpha_t}} \left(x_t - \frac{1 - \alpha_t}{\sqrt{1 - \bar{\alpha}_t}} \epsilon_\theta(x_t, t) \right) + \sqrt{1 - \alpha_{t-1}} \epsilon_t,$$

for $t = T, \dots, 1$, where $\epsilon_\theta(x_t, t)$ is trained to minimize the prediction error between the true and the predicted noise.

3.2. Intuition and Limitations in Reconstruction-Based Detection

Let $\mathcal{X} \subseteq \mathbb{R}^{3 \times 256 \times 256}$ denote the space of all natural images, and \mathcal{M} represent the manifold of images generated by a given pre-trained diffusion model. In general, \mathcal{M} does not coincide with \mathcal{X} , as the model’s learned distribution cannot perfectly align with the true image distribution. However, as generative models become increasingly expressive, \mathcal{M} tends to approximate \mathcal{X} more closely, forming a high-fidelity submanifold near the real image space.

The reconstruction can thus be interpreted as a projection of an input image x onto the generative manifold \mathcal{M} , followed by a stochastic perturbation¹:

$$\mathcal{R}(x) = \Pi_{\mathcal{M}}(x) + \delta(x), \quad (1)$$

where $\mathcal{R}(\bullet)$ denotes the reconstruction operator, $\Pi_{\mathcal{M}}(x)$ denotes the projection of x onto \mathcal{M} , and $\delta(x)$ is a perturbation term capturing the randomness introduced during the reconstruction.

Consequently, for a synthetic image $x \in \mathcal{M}$, its projection onto \mathcal{M} equals x itself, resulting in a reconstruction error of

$$\Delta_{\text{fake}}(x) = |\delta(x)|, \quad (2)$$

¹Similar interpretations have been proposed in the context of LLM-generated text detection [98].

where the absolute value is taken elementwise. In contrast, for a real image $x \in \mathcal{X}$, its reconstruction error is given by

$$\Delta_{\text{real}}(x) = |x - \Pi_{\mathcal{M}}(x) - \delta(x)|. \quad (3)$$

When the generative model is weak, the discrepancy between \mathcal{M} and \mathcal{X} is large, so $|x - \Pi_{\mathcal{M}}(x)|$ dominates the reconstruction error. As a result, the real image achieves a much larger reconstruction error than the synthetic image (see the upper panel of Figure 1 for an illustration), and we classify an image as synthetic if its reconstruction error is small. This explains the rationale behind existing reconstruction-based methods. When the generative model is strong, however, the real and synthetic image distributions are closely aligned, so the signal $|x - \Pi_{\mathcal{M}}(x)|$ becomes small. Consequently, the reconstruction errors of both real and synthetic images are dominated by the perturbation and become similar (see the bottom panel of Figure 1), and existing reconstruction-based methods struggle to distinguish real from synthetic images.

In summary, existing reconstruction-based methods are limited in settings where synthetic images closely resemble real ones, due to the strong capacity of modern generative models. This indicates that relying solely on first-order differences is insufficient in such challenging scenarios, which motivates our difference-in-difference approach that seeks higher-order differences to remove perturbation errors while amplifying the weak signal. We will demonstrate how DID addresses this challenge in the next section.

3.3. Difference-In-Differences

Unlike existing methods which conduct reconstruction only once, DID performs two consecutive reconstructions using the same pre-trained diffusion model:

$$x' = \mathcal{R}(x), \quad x'' = \mathcal{R}(x'),$$

where $\mathcal{R}(\bullet)$ is the reconstruction operator defined in (1), x' denotes the reconstruction of the input image x and x'' denotes the reconstruction of the reconstructed image.

Taking the difference between x' and x yields the first-order reconstruction error, $\Delta(x) = |x - \mathcal{R}(x)|$, which forms the basis of existing reconstruction-based detectors for classification. However, as discussed in the previous section, relying solely on the first-order reconstruction error is limited when the signal $|x - \Pi_{\mathcal{M}}(x)|$ for a real image is small, causing the reconstruction error to be dominated by the perturbation $\delta(x)$. To address this limitation, DID computes the second-order difference between the two reconstruction errors:

$$\Delta^2(x) = |x - x'| - |x' - x''|. \quad (4)$$

To illustrate the intuition behind DID, note that, similar to (2) and (3), one can derive that for a synthetic image x , the

second-order reconstruction error is given by

$$\Delta_{\text{fake}}^2(x) = |\delta(x)| - |\delta(x')|, \quad (5)$$

whereas for a real image, it is

$$\Delta_{\text{real}}^2(x) = |x - \Pi_{\mathcal{M}}(x) - \delta(x)| - |\delta(x')|. \quad (6)$$

When the signal is weak, x is close to x' . In this case, if the perturbation error δ is highly correlated across space, then $\delta(x) \approx \delta(x')$. As a result, the two perturbations cancel out, and (5) and (6) simplify to

$$\Delta_{\text{fake}}^2(x) \approx 0, \quad (7)$$

and

$$|\Delta_{\text{real}}^2(x)| = |x - \Pi_{\mathcal{M}}(x) - \delta(x) + \delta(x')| \approx |x - \Pi_{\mathcal{M}}(x)|, \quad (8)$$

where the first equality holds because the weak signal makes the magnitude of $|x - \Pi_{\mathcal{M}}(x)|$ much smaller than that of $|\delta(x)|$, so that the sign of $x - \Pi_{\mathcal{M}}(x) - \delta(x)$ is dominated by that of $-\delta(x)$.

Comparing (7) and (8) with (2) and (3), it becomes clear that, unlike the first-order difference, the second-order difference is no longer confounded by the perturbation error and depends only on the signal, even when it is weak. This highlights the advantage of DID over existing reconstruction-based algorithms: by taking a second-order difference, it effectively removes the perturbation noise and uncovers the subtle signal.

3.4. Our Proposal

We present the details of our proposed method in this section. Based on the aforementioned analysis, the first-order reconstruction error $\Delta(x) = |x - x'|$ is effective for distinguishing real from synthetic images when their discrepancy is large, whereas the second-order reconstruction error $\Delta^2(x) = |x - x'| - |x' - x''|$ remains reliable when real and synthetic images are highly similar. To handle both cases simultaneously, our detector integrates both first- and second-order reconstruction errors for robust detection (Figure 3); more visualizations are reported in the Appendix Section 12.

Specifically, we train two classifiers independently based on $\Delta(x)$ and $\Delta^2(x)$, respectively, using the standard cross-entropy loss:

$$\mathcal{L} = -\frac{1}{N} \sum_{i=1}^N [y_i \log(y'_i) + (1 - y_i) \log(1 - y'_i)], \quad (9)$$

where y_i denotes the ground-truth label indicating whether the image is real or synthetic, y'_i is the predicted probability produced by the classifier, and N is the number of training samples.

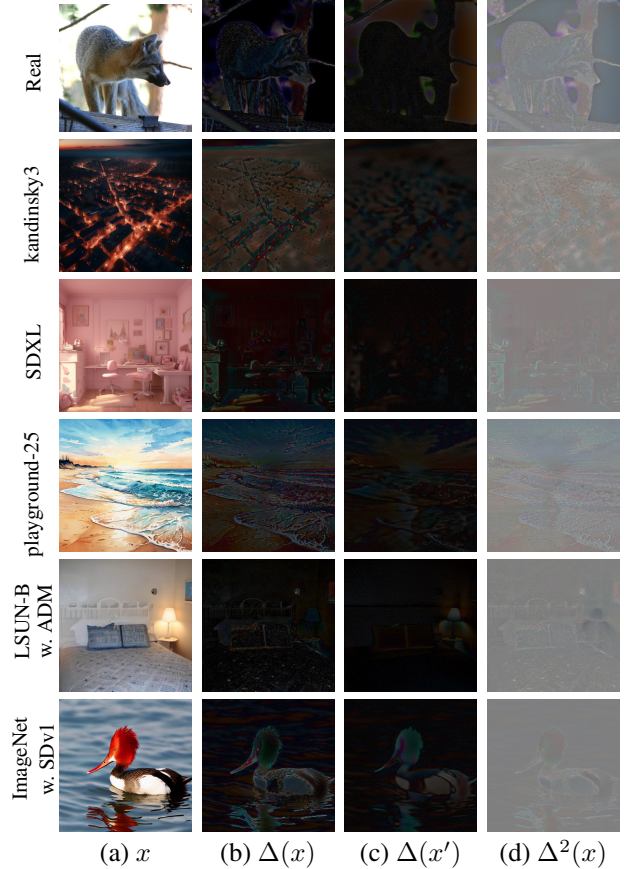


Figure 3. Visualizations of (a) input image x ; (b) its first-order reconstruction error $\Delta(x)$; (c) the reconstruction error of the reconstructed image x' ; and (d) the second-order reconstruction error $\Delta^2(x)$. Compared to the first-order error $\Delta(x)$, the second-order error $\Delta^2(x)$ better distinguishes real from fake images: real images produce more stable and brighter responses, while fake images exhibit noticeably weaker signals, resulting in a larger gap between the two categories.

Each classifier outputs a numerical probability score and predicts an image as real if the score is smaller than a pre-defined threshold c . Finally, an image is classified as real only when both classifiers identify it as real.

4. Experiments

In this section, we conduct extensive numerical experiments to investigate the finite-sample performance of the proposed detector. We begin by describing the experimental setting in Section 4.1. We next report the results of our detector and compare its performance against existing state-of-the-art detectors in Section 4.2 and Appendix Section 9. Finally, we conduct a sensitivity analysis and an ablation study to examine the robustness of our detector and the contribution of the second-order difference in Sections 4.3 and 4.4, respectively.

Table 1. Accuracy (%) of different detectors when trained on **ImageNet & ADM**. The best results are highlighted in **bold**, while the second best results are underlined. All averages are computed from the raw values and then rounded to two decimals.

Train set & Gen. model		ImageNet & ADM				
Eval set	Gen. model	DID	DIRE	LaRE ²	AERO.	UFD
LSUN-B	ADM	99.5	99.5	50.0	52.3	<u>63.9</u>
	PNDM	97.6	97.6	55.4	49.5	<u>91.8</u>
	DDPM	<u>99.5</u>	99.8	56.6	56.7	76.5
	iDDPM	<u>99.4</u>	99.6	50.0	50.3	85.1
	SDv1	<u>99.7</u>	<u>99.9</u>	100	50.6	94.5
	Avg.	<u>99.12</u>	99.25	62.39	51.87	82.36
ImageNet	ADM	100	100	100	51.0	<u>85.8</u>
	SDv1	99.3	98.9	<u>99.2</u>	37.0	79.9
	Avg.	99.64	99.44	<u>99.60</u>	43.99	82.80
LAION	Kan.3	99.5	<u>99.3</u>	64.5	66.7	72.6
	SDXL	99.6	<u>99.4</u>	66.4	55.5	69.5
	Vega	99.7	<u>99.5</u>	66.4	52.2	68.6
	Playground v2.5	99.8	99.8	66.0	53.1	<u>82.8</u>
	Stable Cascade	99.6	<u>99.4</u>	66.3	73.4	81.4
	Avg.	99.60	<u>99.45</u>	65.89	60.14	75.95
Total average		99.41	<u>99.37</u>	70.05	54.00	79.35

4.1. Experimental Setup

To comprehensively evaluate the effectiveness of each detector, we consider a variety of datasets and generative models. Our evaluation benchmark closely follows those used in DIRE [80], FIRE [19], and FakeInversion [16]. Specifically, we use two datasets – ImageNet [24] and LAION [68] – to train the classifier for each detector, with one large-scale training set (40k real and 40k synthetic images) and one smaller set (10k real and 10k synthetic images). For ImageNet, we randomly sample 40,000 real images and 40,000 synthetic images generated by ADM [25]. For LAION, we randomly sample 10,000 real images and generate 10,000 synthetic images using open-source text-to-image models such as Kandinsky 3.0 [2] and SDXL [62], with prompts collected from Midjourney.

For testing, it is crucial to evaluate each detector on unseen datasets to assess how well it generalizes. Therefore, we use three test datasets – LAION [68], ImageNet [24], and LSUN-Bedroom [91] (which is excluded from training) – and generate synthetic images using a more diverse set of generative models than those used in training, including ADM [25], PNDM [46], DDPM [33], iDDPM [56], SDv1 [65], Segmind Vega [32], Playground v2.5 [42], Stable Cascade [61]. Further details on dataset construction and data setup are reported to the Appendix Section 6.

We use the ADM model pretrained on LSUN-Bedroom to obtain the reconstructed image. After obtaining the two

reconstructions, both the first- and second-order differences are fed into a ResNet-50 classifier for detection. All input images are resized to 256×256 . For all baseline detectors, the classification threshold is fixed at the default level $c = 0.5$. Our method, however, uses two classifiers and labels an input as real only when both classifiers predict it as real. To allow for a fair comparison, we set the threshold of each classifier in DID to $1 - \sqrt{0.5} \approx 0.29$, so that its overall false positive rate matches that of using a single classifier with a threshold of 0.5. Accuracy (ACC) is reported as the primary evaluation metric. All our experiments are run on NVIDIA H800 GPUs; the computation and memory cost is reported in the Appendix Section 10.

4.2. Comparison against Existing Baselines

We compare our proposal against the following five state-of-the-art algorithms, using their official open-source implementations for both training and inference. These baseline methods include four reconstruction-based algorithms – (i) DIRE [80], (ii) LaRE² [49], and (iii) AEROBLADE [64] (denoted as AERO.) – as well as (iv) a non-reconstruction-based approach, UniversalFakeDetect (denoted as UFD) [58], which leverages a feature space not explicitly trained to distinguish real from synthetic images. Further details for our method and all baselines are reported in the Appendix Section 7.

Table 2. Accuracy (%) of different detectors when trained on **LAION & Kan.3** (left block) and **LAION & SDXL** (right block). The best results are highlighted in **bold**, while the second best results are underlined. All averages are computed from the raw values and then rounded to two decimals. The last column of each block reports the improvement of DID over the second-best baseline.

Train set & Gen. model		LAION & Kan.3					Imp.	LAION & SDXL					Imp.
Eval set	Gen. model	DID	DIRE	LaRE ²	AERO.	UFD		DID	DIRE	LaRE ²	AERO.	UFD	
LSUN-B	ADM	90.7	<u>88.1</u>	50.3	50.0	50.8	21.85%	95.0	<u>94.3</u>	50.2	50.0	50.3	13.04%
	PNDM	78.2	<u>73.5</u>	71.2	49.8	51.5	17.55%	81.7	<u>74.6</u>	51.6	49.8	50.9	27.95%
	DDPM	88.7	<u>85.2</u>	56.5	56.4	51.5	24.05%	95.1	<u>93.3</u>	57.1	56.4	50.5	27.73%
	iDDPM	80.1	<u>77.5</u>	50.0	49.8	54.2	11.33%	89.0	<u>86.8</u>	50.0	49.8	53.3	16.29%
	SDv1	<u>98.6</u>	97.8	99.9	49.8	49.7	-	<u>98.4</u>	98.3	99.7	49.8	50.5	-
	Avg.		87.25	<u>84.41</u>	65.56	51.13	51.52	18.23%	91.83	<u>89.44</u>	61.70	51.13	51.09
ImageNet	ADM	99.1	<u>96.7</u>	89.5	50.7	58.7	74.03%	99.6	<u>96.3</u>	93.3	50.7	61.1	89.65%
	SDv1	99.2	<u>97.7</u>	94.4	35.0	65.4	65.33%	99.1	<u>96.1</u>	95.5	35.0	67.3	75.73%
	Avg.		99.16	<u>97.16</u>	91.91	42.83	62.03	70.46%	99.34	<u>96.22</u>	94.40	42.83	64.18
LAION	Kan.3	100	100	100	58.7	<u>93.7</u>	-	99.8	<u>99.3</u>	97.6	58.7	92.9	64.29%
	SDXL	100	<u>99.9</u>	99.4	52.5	87.0	100%	99.9	99.9	99.9	52.5	<u>92.3</u>	-
	Vega	100	<u>99.4</u>	95.5	51.0	79.9	100%	99.9	<u>99.8</u>	99.7	51.0	83.8	50.00%
	Playground v2.5	100	100	<u>97.9</u>	51.1	93.2	-	99.9	99.9	<u>99.4</u>	51.1	93.3	-
	Stable Cascade	100	100	<u>99.6</u>	64.7	95.7	-	99.8	<u>99.5</u>	<u>99.5</u>	64.7	95.4	54.55%
	Avg.		100	<u>99.84</u>	98.45	55.57	89.87	100%	99.84	<u>99.67</u>	99.20	55.57	91.50
Total average		94.55	<u>92.96</u>	83.66	51.60	69.25	22.52%	96.42	<u>94.83</u>	82.78	51.60	70.11	30.66%

Performance with a Larger Training Dataset. When trained on the ImageNet dataset with 40k real images and 40k synthetic images generated by ADM, we report the accuracy of different detectors in Table 1. DID achieves performance very similar to DIRE. This is expected for two reasons. First, the training dataset contains a large number of samples. Second, we also use ADM for reconstruction, so the generative model used to produce the synthetic training images aligns with the one used for reconstruction. Under this large-sample and well-aligned setting, the first-order reconstruction error is already highly discriminative for distinguishing real from AI-generated images. As a result, both DID and DIRE achieve classification accuracy close to 100%. In contrast, other methods such as AEROBLADE, LaRE² and UFD may perform competitively on certain datasets but are less robust across datasets, and their accuracy generally falls behind both DIRE and our DID.

Performance with a Smaller Training Dataset. We report the accuracy of various detectors trained on the LAION dataset in Table 2. This represents a more challenging setting for two reasons: (i) the sample size is smaller, with only 10k real and 10k synthetic images; (ii) the generators used to create the synthetic training datasets (Kan3 and SDXL) differ from the ADM model used for reconstruction.

In such cases, the first-order reconstruction discrepancy alone is no longer sufficiently reliable. Consequently, DID benefits from its second-order reconstruction error and outperforms DIRE in almost all settings, particularly when evaluated on LSUN-B and ImageNet, where the test images differ from the training dataset LAION. Across these cases, our total improvement ranges from 20–30%. This demonstrates that our second-order reconstruction error plays a crucial role in more complex tasks, especially when the sample size is smaller or when the generator differs from the reconstruction model. Other baseline detectors, such as LaRE² and UFD, perform well when the training and testing datasets are the same, but their performance drops significantly when the datasets differ. This demonstrates their limited generalization ability. AERO. also fails in most cases.

4.3. Sensitivity Analysis

In Section 4.2, all synthetic images were generated using diffusion models. In this section, we further evaluate each detector’s generalization ability by testing it on images produced by generative adversarial networks (GANs). We consider three GAN models, such as StyleGAN, ProjectedGAN, and Diff-ProjectedGAN, and report the ACC of each detector in Table 3. Although our model is trained

Table 3. Detection accuracy (%) on GAN-generated images under different training settings. Best in **bold**, second best underlined. All averages are computed from the raw values and then rounded to two decimals. The last column reports the improvement of DID over the second-best baseline.

Train set & Gen. model	Eval set	Gen. model	Accuracy (%)					Imp.
			DID	DIRE	LaRE ²	AERO.	UFD	
LAION & Kan.3	LSUN-B	StyleGAN	95.8	<u>94.3</u>	50.4	49.8	50.8	26.32%
		ProjectedGAN	93.4	<u>91.0</u>	51.2	49.8	50.7	26.52%
		Diff-ProjectedGAN	92.7	<u>90.2</u>	51.9	49.8	51.1	25.51%
		Avg.	93.95	<u>91.82</u>	51.12	49.75	50.85	26.07%
LAION & SDXL	LSUN-B	StyleGAN	96.8	<u>96.3</u>	50.7	49.8	50.9	12.16%
		ProjectedGAN	94.8	<u>93.8</u>	52.8	49.8	50.9	16.13%
		Diff-ProjectedGAN	93.1	<u>92.1</u>	53.6	49.8	50.9	12.66%
		Avg.	94.88	<u>94.07</u>	52.37	49.75	50.88	13.76%
Total average			94.42	<u>92.94</u>	51.74	49.75	50.87	20.90%

exclusively on diffusion-generated data from “Kandinsky3” or “SDXL,” it consistently achieves the highest accuracy across all three GAN variants. In every setting, our method outperforms DIRE, with improvements of up to 20.90%. The performance gap becomes even more pronounced when compared with LaRE², and AEROBLADE, all of which fail to generalize to these GAN-generated distributions. UniversalFakeDetect also struggles in this scenario. These results demonstrate that our detector – despite being trained solely on diffusion-generated images – remains robust to synthetic images produced by substantially different generative mechanisms. We also conduct a complementary sensitivity analysis on image formats (JPEG vs. PNG); details are provided in the Appendix Section 8.

4.4. Ablation Study

In this section, we conduct an ablation study to compare our DID with a variant (denoted as Δ^2) that uses only the second-order reconstruction error and excludes the first-order term. For completeness, we also include DIRE as a reference. To facilitate the computation, we train a lightweight model using only 10% of the LAION training data and report the results in Table 4.

We make several observations. First, in most settings, Δ^2 outperforms DIRE, demonstrating that second-order differences are more effective than first-order differences at capturing subtle discrepancies between real and synthetic images. Second, in settings where LSUN is used as the evaluation dataset and synthetic images are generated by ADM, DIRE outperforms Δ^2 . A closer inspection reveals that this corresponds to a simple scenario in which the synthetic images are produced by the same model used for reconstruction. This is consistent with our analysis in Section 3, which shows that first-order differences are sufficient in simpler

Table 4. Accuracy (%) on various evaluation datasets when trained on LAION & Kan3.

Eval set	Gen. model	Accuracy (%)		
		DID	Δ^2	DIRE
LSUN-B	ADM	86.5	69.0	84.0
	PNDM	83.0	81.5	67.5
	DDPM	82.0	78.0	71.5
ImageNet	ADM	98.9	98.4	91.0
	SDv1	98.9	98.7	93.5
LAION	Kan.3	99.9	100	99.9
	SDXL	99.9	99.9	99.2
	Vega	99.9	99.9	98.8

settings. Finally, DID outperforms or performs comparably to both Δ^2 and DIRE across all settings, illustrating the advantages of leveraging both first- and second-order differences for classification. Additional ablations on the fusion strategy are reported in the Appendix Section 11.

5. Discussion

This paper studies the detection of AI-generated images. A popular approach is reconstruction-based, which relies on the first-order difference between an input image and its reconstruction as the basis for classification. Although these algorithms perform well when real and AI-generated images differ substantially, they often fail when the two appear highly similar. To address this challenge, we propose a difference-in-difference approach that utilizes a second-order difference. Our analysis in Section 3.3 shows that the second-order difference effectively removes perturba-

tion noise and uncovers subtle discrepancies between real and AI-generated images. We then integrate both first- and second-order differences into our classifier to simultaneously handle both settings. Extensive experiments demonstrate that our detector outperforms state-of-the-art algorithms (Section 4.2); an sensitivity analysis shows that its performance is robust across different generative models (Section 4.3); and an ablation study confirms the critical role of the second-order difference (Section 4.4).

We focus on using second-order differences for detection, but our idea naturally extends to even higher-order differences. For example, one may define a third-order difference as

$$\Delta^3(x) = |\Delta^2(x) - \Delta^2(x')|, \quad (10)$$

for an input image x and its reconstruction x' . In principle, one could incorporate all higher-order differences into the classifier to capture weak signals. However, computing a K -th-order difference requires reconstructing the image K times, which significantly increases the computation. Thus, there is an inherent trade-off: higher-order differences may uncover more subtle discrepancies between real and AI-generated images, but at the cost of reduced computational efficiency. Determining the optimal order that balances detection performance and computational cost remains an open question for our future work.

Finally, we note that although DID is proposed for detecting AI-generated images, the same principle can be readily generalized to the detection of LLM-generated text [see e.g., 8, 53, 97, 99].

Acknowledgements

Qi, Zhou, and Yang’s research was supported by the National Natural Science Foundation of China (NSFC) under Grant No. 12271286.

References

- [1] Joshua D Angrist and Jörn-Steffen Pischke. *Mostly harmless econometrics: An empiricist’s companion*. Princeton university press, 2009. 3
- [2] Vladimir Arkhipkin, Andrei Filatov, Viacheslav Vasilev, Anastasia Maltseva, Said Azizov, Igor Pavlov, Julia Agafonova, Andrey Kuznetsov, and Denis Dimitrov. Kandinsky 3.0 technical report. *arXiv preprint arXiv:2312.03511*, 2023. 1, 6
- [3] Orley C Ashenfelter and David Card. Using the longitudinal structure of earnings to estimate the effect of training programs, 1984. 3
- [4] Jason Baldrige, Jakob Bauer, Mukul Bhutani, Nicole Brichtova, Andrew Bunner, Lluís Castrejon, Kelvin Chan, Yichang Chen, Sander Dieleman, Yuqing Du, et al. Imagen 3. *arXiv preprint arXiv:2408.07009*, 2024. 1
- [5] Quentin Bammey. Synthbuster: Towards detection of diffusion model generated images. *IEEE Open Journal of Signal Processing*, 5:1–9, 2023. 3
- [6] Hmrishav Bandyopadhyay, Rahim Entezari, Jim Scott, Reshith Adithyan, Yi-Zhe Song, and Varun Jampani. Sd3. 5-flash: Distribution-guided distillation of generative flows. *arXiv preprint arXiv:2509.21318*, 2025. 1
- [7] Fan Bao, Chongxuan Li, Jun Zhu, and Bo Zhang. Analytic-dpm: an analytic estimate of the optimal reverse variance in diffusion probabilistic models. *arXiv preprint arXiv:2201.06503*, 2022. 3
- [8] Guangsheng Bao, Yanbin Zhao, Zhiyang Teng, Linyi Yang, and Yue Zhang. Fast-detectgpt: Efficient zero-shot detection of machine-generated text via conditional probability curvature. In *The Twelfth International Conference on Learning Representations*, 2024. 9
- [9] James Betker, Gabriel Goh, Li Jing, Tim Brooks, Jianfeng Wang, Linjie Li, Long Ouyang, Juntang Zhuang, Joyce Lee, Yufei Guo, et al. Improving image generation with better captions. *Computer Science*. <https://cdn.openai.com/papers/dall-e-3.pdf>, 2(3):8, 2023. 1
- [10] Richard Blundell and Monica Costa Dias. Alternative approaches to evaluation in empirical microeconomics. *Journal of human resources*, 44(3):565–640, 2009. 3
- [11] Ali Borji. Qualitative failures of image generation models and their application in detecting deepfakes. *Image and Vision Computing*, 137:104771, 2023. 3
- [12] Valentin De Bortoli, Emile Mathieu, Michael J. Hutchinson, James Thornton, Yee Whye Teh, and A. Doucet. Riemannian score-based generative modeling. *ArXiv*, abs/2202.02763, 2022. 3
- [13] Brantly Callaway and Pedro HC Sant’Anna. Difference-in-differences with multiple time periods. *Journal of econometrics*, 225(2):200–230, 2021. 3
- [14] Donald T Campbell and Julian C Stanley. *Experimental and quasi-experimental designs for research*. Ravenio books, 2015. 3
- [15] David Card and Alan B Krueger. Minimum wages and employment: A case study of the fast food industry in new jersey and pennsylvania, 1993. 3
- [16] George Cazenavette, Avneesh Sud, Thomas Leung, and Ben Usman. Fakeinversion: Learning to detect images from unseen text-to-image models by inverting stable diffusion. In *Proceedings of the IEEE/CVF Conference on Computer Vision and Pattern Recognition*, pages 10759–10769, 2024. 3, 6
- [17] Baoying Chen, Jishen Zeng, Jianquan Yang, and Rui Yang. Drct: Diffusion reconstruction contrastive training towards universal detection of diffusion generated images. In *Forty-first International Conference on Machine Learning*, 2024. 3
- [18] Ruoxin Chen, Junwei Xi, Zhiyuan Yan, Ke-Yue Zhang, Shuang Wu, Jingyi Xie, Xu Chen, Lei Xu, Isabel Guan, Taiping Yao, and Shouhong Ding. Dual data alignment makes AI-generated image detector easier generalizable. In *The Thirty-ninth Annual Conference on Neural Information Processing Systems*, 2025. 3
- [19] Beilin Chu, Xuan Xu, Xin Wang, Yufei Zhang, Weike You, and Linna Zhou. Fire: Robust detection of diffusion-generated images via frequency-guided reconstruction er-

- ror. In *Proceedings of the Computer Vision and Pattern Recognition Conference*, pages 12830–12839, 2025. 2, 3, 6
- [20] Umur Aybars Ciftci, Ilke Demir, and Lijun Yin. Fake-catcher: Detection of synthetic portrait videos using biological signals. *IEEE transactions on pattern analysis and machine intelligence*, 2020. 3
- [21] Roberto Corvi, Ruben Tolosana, Ruben Vera-Rodriguez, Joshua Harvill, Ulrich Scherhag, and Naser Damer. Intriguing properties of synthetic images: From generative adversarial networks to diffusion models. In *IEEE/CVF Conference on Computer Vision and Pattern Recognition Workshops (CVPRW)*, pages 4173–4182. IEEE, 2023. 2
- [22] Davide Cozzolino, Giovanni Poggi, Matthias Nießner, and Luisa Verdoliva. Zero-shot detection of ai-generated images. In *European Conference on Computer Vision*, pages 54–72. Springer, 2024. 3
- [23] Katherine Crowson, Stella Biderman, Daniel Kornis, Dashiell Stander, Eric Hallahan, Louis Castricato, and Edward Raff. Vqgan-clip: Open domain image generation and editing with natural language guidance. In *European conference on computer vision*, pages 88–105. Springer, 2022. 2
- [24] Jia Deng, Wei Dong, Richard Socher, Li-Jia Li, Kai Li, and Li Fei-Fei. Imagenet: A large-scale hierarchical image database. In *2009 IEEE conference on computer vision and pattern recognition*, pages 248–255. Ieee, 2009. 6, 1, 8
- [25] Prafulla Dhariwal and Alexander Nichol. Diffusion models beat gans on image synthesis. *Advances in neural information processing systems*, 34:8780–8794, 2021. 3, 6, 1
- [26] Tim Dockhorn, Arash Vahdat, and Karsten Kreis. Gennie: Higher-order denoising diffusion solvers. *Advances in Neural Information Processing Systems*, 35:30150–30166, 2022. 3
- [27] Hany Farid. Perspective (in) consistency of paint by text. *arXiv preprint arXiv:2206.14617*, 2022. 3
- [28] Joel Frank, Thorsten Eisenhofer, Lea Schönherr, Asja Fischer, Dorothea Kolossa, and Thorsten Holz. Leveraging frequency analysis for deep fake image recognition. In *Proceedings of the 38th International Conference on Machine Learning (ICML)*, pages 3247–3258. PMLR, 2020. 2
- [29] Shansan Gong, Mukai Li, Jiangtao Feng, Zhiyong Wu, and LingPeng Kong. Diffuseq: Sequence to sequence text generation with diffusion models. *arXiv preprint arXiv:2210.08933*, 2022. 3
- [30] Andrew Goodman-Bacon. Difference-in-differences with variation in treatment timing. *Journal of econometrics*, 225(2):254–277, 2021. 3
- [31] Shuyang Gu, Dong Chen, Jianmin Bao, Fang Wen, Bo Zhang, Dongdong Chen, Lu Yuan, and Baining Guo. Vector quantized diffusion model for text-to-image synthesis. In *Proceedings of the IEEE/CVF conference on computer vision and pattern recognition*, pages 10696–10706, 2022. 2
- [32] Yatharth Gupta, Vishnu V Jaddipal, Harish Prabhala, Sayak Paul, and Patrick Von Platen. Progressive knowledge distillation of stable diffusion xl using layer level loss. *arXiv preprint arXiv:2401.02677*, 2024. 6, 1
- [33] Jonathan Ho, Ajay Jain, and Pieter Abbeel. Denoising diffusion probabilistic models. *Advances in neural information processing systems*, 33:6840–6851, 2020. 2, 6
- [34] Jonathan Ho, William Chan, Chitwan Saharia, Jay Whang, Ruiqi Gao, Alexey Gritsenko, Diederik P Kingma, Ben Poole, Mohammad Norouzi, David J Fleet, et al. Imagen video: High definition video generation with diffusion models. *arXiv preprint arXiv:2210.02303*, 2022. 2
- [35] Chin-Wei Huang, Milad Aghajohari, Joey Bose, Prakash Panangaden, and Aaron C Courville. Riemannian diffusion models. *Advances in Neural Information Processing Systems*, 35:2750–2761, 2022. 3
- [36] Shaohan Huang, Li Dong, Wenhui Wang, Yaru Hao, Saksham Singhal, Shuming Ma, Tengchao Lv, Lei Cui, Owais Khan Mohammed, Barun Patra, et al. Language is not all you need: Aligning perception with language models. *Advances in Neural Information Processing Systems*, 36:72096–72109, 2023. 2
- [37] Ray Hyman. Quasi-experimentation: Design and analysis issues for field settings (book). *Journal of Personality Assessment*, 46(1):96–97, 1982. 3
- [38] Jaehyeong Jo, Seul Lee, and Sung Ju Hwang. Score-based generative modeling of graphs via the system of stochastic differential equations. In *International conference on machine learning*, pages 10362–10383. PMLR, 2022. 3
- [39] Tero Karras, Miika Aittala, Timo Aila, and Samuli Laine. Elucidating the design space of diffusion-based generative models. *Advances in neural information processing systems*, 35:26565–26577, 2022. 3
- [40] Diederik Kingma, Tim Salimans, Ben Poole, and Jonathan Ho. Variational diffusion models. *Advances in neural information processing systems*, 34:21696–21707, 2021. 3
- [41] Romeo Lanzino, Federico Fontana, Anxhelo Diko, Marco Raoul Marini, and Luigi Cinque. Faster than lies: Real-time deepfake detection using binary neural networks. In *Proceedings of the IEEE/CVF Conference on Computer Vision and Pattern Recognition*, pages 3771–3780, 2024. 3
- [42] Daiqing Li, Aleks Kamko, Ehsan Akhgari, Ali Sabet, Linmiao Xu, and Suhail Doshi. Playground v2. 5: Three insights towards enhancing aesthetic quality in text-to-image generation. *arXiv preprint arXiv:2402.17245*, 2024. 6, 1
- [43] Chen-Hsuan Lin, Jun Gao, Luming Tang, Towaki Takikawa, Xiaohui Zeng, Xun Huang, Karsten Kreis, Sanja Fidler, Ming-Yu Liu, and Tsung-Yi Lin. Magic3d: High-resolution text-to-3d content creation. In *Proceedings of the IEEE/CVF conference on computer vision and pattern recognition*, pages 300–309, 2023. 2
- [44] Kaiqing Lin, Zhiyuan Yan, Ruoxin Chen, Junyan Ye, Keyue Zhang, Yue Zhou, Peng Jin, Bin Li, Taiping Yao, and Shouhong Ding. Seeing before reasoning: A unified framework for generalizable and explainable fake image detection. *arXiv preprint arXiv:2509.25502*, 2025. 3
- [45] Li Lin, Neeraj Gupta, Yue Zhang, Hainan Ren, Chun-Hao Liu, Feng Ding, Xin Wang, Xin Li, Luisa Verdoliva, and Shu Hu. Detecting multimedia generated by large ai models: A survey. *arXiv preprint arXiv:2402.00045*, 2024. 3

- [46] Luping Liu, Yi Ren, Zhijie Lin, and Zhou Zhao. Pseudo numerical methods for diffusion models on manifolds. *arXiv preprint arXiv:2202.09778*, 2022. 6
- [47] Peter Lorenz, Ricard L Durall, and Janis Keuper. Detecting images generated by deep diffusion models using their local intrinsic dimensionality. In *Proceedings of the IEEE/CVF International Conference on Computer Vision*, pages 448–459, 2023. 3
- [48] Cheng Lu, Kaiwen Zheng, Fan Bao, Jianfei Chen, Chongxuan Li, and Jun Zhu. Maximum likelihood training for score-based diffusion odes by high order denoising score matching. In *International conference on machine learning*, pages 14429–14460. PMLR, 2022. 3
- [49] Yuhang Luo, Jing Du, Kaizhe Yan, and Shengyu Ding. Lare²: Latent reconstruction error based method for diffusion-generated image detection. In *Proceedings of the IEEE/CVF Conference on Computer Vision and Pattern Recognition (CVPR)*, pages 17006–17015. IEEE, 2024. 2, 3, 6
- [50] Ruipeng Ma, Jinhao Duan, Fei Kong, Xiaoshuang Shi, and Kaidi Xu. Exposing the fake: Effective diffusion-generated images detection. *arXiv preprint arXiv:2307.06272*, 2023. 3
- [51] Scott McCloskey and Michael Albright. Detecting gan-generated imagery using color cues. *arXiv preprint arXiv:1812.08247*, 2018. 3
- [52] Scott McCloskey and Michael Albright. Detecting gan-generated imagery using saturation cues. In *2019 IEEE international conference on image processing (ICIP)*, pages 4584–4588. IEEE, 2019. 3
- [53] Eric Mitchell, Yoonho Lee, Alexander Khazatsky, Christopher D Manning, and Chelsea Finn. Detectgpt: Zero-shot machine-generated text detection using probability curvature. In *International conference on machine learning*, pages 24950–24962. PMLR, 2023. 9
- [54] Minh-Quang Nguyen, Khanh-Duy Ho, Hoang-Minh Nguyen, Canh-Minh Tu, Minh-Triet Tran, and Trong-Le Do. Unmasking the artist: Discriminating human-drawn and ai-generated human face art through facial feature analysis. In *2023 International Conference on Multimedia Analysis and Pattern Recognition (MAPR)*, pages 1–6. IEEE, 2023. 3
- [55] Alex Nichol, Prafulla Dhariwal, Aditya Ramesh, Pranav Shyam, Pamela Mishkin, Bob McGrew, Ilya Sutskever, and Mark Chen. Glide: Towards photorealistic image generation and editing with text-guided diffusion models. *arXiv preprint arXiv:2112.10741*, 2021. 2
- [56] Alexander Quinn Nichol and Prafulla Dhariwal. Improved denoising diffusion probabilistic models. In *International conference on machine learning*, pages 8162–8171. PMLR, 2021. 3, 6
- [57] Chenhao Niu, Yang Song, Jiaming Song, Shengjia Zhao, Aditya Grover, and Stefano Ermon. Permutation invariant graph generation via score-based generative modeling. In *International conference on artificial intelligence and statistics*, pages 4474–4484. PMLR, 2020. 3
- [58] Utkarsh Ojha, Yuheng Li, and Yong Jae Lee. Towards universal fake image detectors that generalize across generative models, 2024. 6
- [59] OpenAI. Video generation models as world simulators. <https://openai.com/index/video-generation-models-as-world-simulators/>, 2024. Technical report. 2
- [60] William Peebles and Saining Xie. Scalable diffusion models with transformers. In *Proceedings of the IEEE/CVF international conference on computer vision*, pages 4195–4205, 2023. 3
- [61] Pablo Pernias, Dominic Rampas, Mats L Richter, Christopher J Pal, and Marc Aubreville. Würstchen: An efficient architecture for large-scale text-to-image diffusion models. *arXiv preprint arXiv:2306.00637*, 2023. 6, 1
- [62] Dustin Podell, Zion English, Kyle Lacey, Andreas Blattmann, Tim Dockhorn, Jonas Müller, Joe Penna, and Robin Rombach. Sdxl: Improving latent diffusion models for high-resolution image synthesis. *arXiv preprint arXiv:2307.01952*, 2023. 2, 6, 1
- [63] Aditya Ramesh, Prafulla Dhariwal, Alex Nichol, Casey Chu, and Mark Chen. Hierarchical text-conditional image generation with clip latents. *arXiv preprint arXiv:2204.06125*, 1(2):3, 2022. 2, 3
- [64] Jonas Ricker, Denis Lukovnikov, and Asja Fischer. Aeroblade: Training-free detection of latent diffusion images using autoencoder reconstruction error. In *Proceedings of the IEEE/CVF Conference on Computer Vision and Pattern Recognition*, pages 9130–9140, 2024. 3, 6
- [65] Robin Rombach, Andreas Blattmann, Dominik Lorenz, Patrick Esser, and Björn Ommer. High-resolution image synthesis with latent diffusion models. In *Proceedings of the IEEE/CVF conference on computer vision and pattern recognition*, pages 10684–10695, 2022. 6
- [66] Nataniel Ruiz, Yuanzhen Li, Varun Jampani, Yael Pritch, Michael Rubinstein, and Kfir Aberman. Dreambooth: Fine tuning text-to-image diffusion models for subject-driven generation. In *Proceedings of the IEEE/CVF conference on computer vision and pattern recognition*, pages 22500–22510, 2023. 2
- [67] Chitwan Saharia, William Chan, Saurabh Saxena, Lala Li, Jay Whang, Emily L Denton, Kamyar Ghasemipour, Raphael Gontijo Lopes, Burcu Karagol Ayan, Tim Salimans, et al. Photorealistic text-to-image diffusion models with deep language understanding. *Advances in neural information processing systems*, 35:36479–36494, 2022. 2
- [68] Christoph Schuhmann, Romain Beaumont, Richard Vencu, Cade Gordon, Ross Wightman, Mehdi Cherti, Theo Coombes, Aarush Katta, Clayton Mullis, Mitchell Wortsman, et al. Laion-5b: An open large-scale dataset for training next generation image-text models. *Advances in neural information processing systems*, 35:25278–25294, 2022. 6, 1
- [69] Shelly Sheynin, Adam Polyak, Uriel Singer, Yuval Kirstain, Amit Zohar, Oron Ashual, Devi Parikh, and Yaniv Taigman. Emu edit: Precise image editing via recognition and generation tasks. In *Proceedings of the IEEE/CVF Conference*

- on *Computer Vision and Pattern Recognition*, pages 8871–8879, 2024. 1
- [70] Jascha Sohl-Dickstein, Eric Weiss, Niru Maheswaranathan, and Surya Ganguli. Deep unsupervised learning using nonequilibrium thermodynamics. In *International conference on machine learning*, pages 2256–2265. pmlr, 2015. 2
- [71] Jiaming Song, Chenlin Meng, and Stefano Ermon. Denoising diffusion implicit models. *arXiv preprint arXiv:2010.02502*, 2020. 3
- [72] Yang Song and Stefano Ermon. Generative modeling by estimating gradients of the data distribution. *Advances in neural information processing systems*, 32, 2019. 2, 3
- [73] Yang Song and Stefano Ermon. Improved techniques for training score-based generative models. *Advances in neural information processing systems*, 33:12438–12448, 2020. 2
- [74] Yang Song, Jascha Sohl-Dickstein, Diederik P Kingma, Abhishek Kumar, Stefano Ermon, and Ben Poole. Score-based generative modeling through stochastic differential equations. *arXiv preprint arXiv:2011.13456*, 2020. 3
- [75] Yang Song, Conor Durkan, Iain Murray, and Stefano Ermon. Maximum likelihood training of score-based diffusion models. *Advances in neural information processing systems*, 34:1415–1428, 2021. 3
- [76] Liyang Sun and Sarah Abraham. Estimating dynamic treatment effects in event studies with heterogeneous treatment effects. *Journal of econometrics*, 225(2):175–199, 2021. 3
- [77] Arash Vahdat, Karsten Kreis, and Jan Kautz. Score-based generative modeling in latent space. *Advances in neural information processing systems*, 34:11287–11302, 2021. 3
- [78] Bram Wallace, Meihua Dang, Rafael Rafailov, Linqi Zhou, Aaron Lou, Senthil Purushwalkam, Stefano Ermon, Caiming Xiong, Shafiq Joty, and Nikhil Naik. Diffusion model alignment using direct preference optimization. In *Proceedings of the IEEE/CVF Conference on Computer Vision and Pattern Recognition*, pages 8228–8238, 2024. 3
- [79] Fei Wang, Xuecheng Wu, Zheng Zhang, Danlei Huang, Yuheng Huang, and Bo Wang. End4: End-to-end denoising diffusion for diffusion-based inpainting detection. *arXiv preprint arXiv:2509.13214*, 2025. Version v2, submitted 18 Sep 2025. 2
- [80] Zhendong Wang, Jianmin Bao, Wengang Zhou, Weilun Wang, Hezhen Hu, Hong Chen, and Houqiang Li. Dire: Diffusion reconstruction error for diffusion-generated image detection. In *Proceedings of the IEEE/CVF International Conference on Computer Vision (ICCV)*, pages 22445–22455. IEEE, 2023. 2, 3, 6, 1
- [81] Daniel Watson, William Chan, Jonathan Ho, and Mohammad Norouzi. Learning fast samplers for diffusion models by differentiating through sample quality. In *International Conference on Learning Representations*, 2021. 3
- [82] Moritz Wolter, Felix Blanke, Raoul Heese, and Jochen Garcke. Wavelet-packets for deepfake image analysis and detection. *Machine Learning*, 111(11):4295–4327, 2022. 3
- [83] Ziyi Xi, Wenmin Huang, Kangkang Wei, Weiqi Luo, and Peijia Zheng. Ai-generated image detection using a cross-attention enhanced dual-stream network. In *2023 Asia Pacific Signal and Information Processing Association Annual Summit and Conference (APSIPA ASC)*, pages 1463–1470. IEEE, 2023. 3
- [84] Jiazheng Xu, Xiao Liu, Yuchen Wu, Yuxuan Tong, Qinkai Li, Ming Ding, Jie Tang, and Yuxiao Dong. Imagereward: Learning and evaluating human preferences for text-to-image generation. *Advances in Neural Information Processing Systems*, 36:15903–15935, 2023. 3
- [85] Zhiyuan Yan, Jiangming Wang, Peng Jin, Ke-Yue Zhang, Chengchun Liu, Shen Chen, Taiping Yao, Shouhong Ding, Baoyuan Wu, and Li Yuan. Orthogonal subspace decomposition for generalizable AI-generated image detection. In *Forty-second International Conference on Machine Learning*, 2025. 3
- [86] Ling Yang, Jingwei Liu, Shenda Hong, Zhilong Zhang, Zhilin Huang, Zheming Cai, Wentao Zhang, and Bin Cui. Improving diffusion-based image synthesis with context prediction. *Advances in Neural Information Processing Systems*, 36:37636–37656, 2023. 3
- [87] Ling Yang, Zhilong Zhang, Yang Song, Shenda Hong, Runsheng Xu, Yue Zhao, Wentao Zhang, Bin Cui, and Ming-Hsuan Yang. Diffusion models: A comprehensive survey of methods and applications. *ACM computing surveys*, 56(4):1–39, 2023. 2
- [88] Ling Yang, Zhaochen Yu, Chenlin Meng, Minkai Xu, Stefano Ermon, and Bin Cui. Mastering text-to-image diffusion: Recaptioning, planning, and generating with multimodal llms. In *Forty-first International Conference on Machine Learning*, 2024. 3
- [89] Ling Yang, Ye Tian, Bowen Li, Xinchen Zhang, Ke Shen, Yunhai Tong, and Mengdi Wang. Mmada: Multimodal large diffusion language models. *arXiv preprint arXiv:2505.15809*, 2025. 2
- [90] Shukang Yin, Chaoyou Fu, Sirui Zhao, Ke Li, Xing Sun, Tong Xu, and Enhong Chen. A survey on multimodal large language models. *National Science Review*, 11(12):nwae403, 2024. 2
- [91] Fisher Yu, Ari Seff, Yinda Zhang, Shuran Song, Thomas Funkhouser, and Jianxiong Xiao. Lsun: Construction of a large-scale image dataset using deep learning with humans in the loop. *arXiv preprint arXiv:1506.03365*, 2015. 6, 1
- [92] Mingyuan Zhang, Zhongang Cai, Liang Pan, Fangzhou Hong, Xinying Guo, Lei Yang, and Ziwei Liu. Motiondiffuse: Text-driven human motion generation with diffusion model. *IEEE transactions on pattern analysis and machine intelligence*, 46(6):4115–4128, 2024. 2
- [93] Qinsheng Zhang and Yongxin Chen. Fast sampling of diffusion models with exponential integrator. *arXiv preprint arXiv:2204.13902*, 2022. 3
- [94] Qinsheng Zhang, Molei Tao, and Yongxin Chen. gddim: Generalized denoising diffusion implicit models. *arXiv preprint arXiv:2206.05564*, 2022. 3
- [95] Xinran Zhang, Sertac Karaman, and Shih-Fu Chang. Detecting gan-synthesized faces using saturation cues. In *IEEE Conference on Computer Vision and Pattern Recognition Workshops (CVPRW)*, pages 3701–3710. IEEE, 2019. 2
- [96] Nan Zhong, Yiran Xu, Sheng Li, Zhenxing Qian, and Xinpeng Zhang. Patchcraft: Exploring texture patch for

- efficient ai-generated image detection. *arXiv preprint arXiv:2311.12397*, 2023. 3
- [97] Hongyi Zhou, Jin Zhu, Pingfan Su, Kai Ye, Ying Yang, Shakeel Gavioli-Akilagun, and Chengchun Shi. Adadetect-gpt: Adaptive detection of llm-generated text with statistical guarantees. In *The Thirty-ninth Annual Conference on Neural Information Processing Systems*, 2025. 9
- [98] Hongyi Zhou, Jin Zhu, Erhan Xu, Kai Ye, Ying Yang, and Chengchun Shi. Learn-to-distance: Distance learning for detecting LLM-generated text. *arXiv preprint arXiv:2601.21895*, 2026. 4
- [99] Hongyi Zhou, Jin Zhu, Ying Yang, and Chengchun Shi. Detecting llm-generated text with performance guarantees. *arXiv preprint arXiv:2601.06586*, 2026. 9
- [100] Ming Zhu, H. Chen, M. Huang, et al. Gendet: Towards good generalizations for ai-generated image detection. *arXiv preprint arXiv:2312.08880*, 2023. 3
- [101] Ming Zhu, H. Chen, Q. Yan, et al. Genimage: A million-scale benchmark for detecting ai-generated image. *Advances in Neural Information Processing Systems*, 36: 77771–77782, 2023. 3

A Difference-in-Difference Approach to Detecting AI-Generated Images

Supplementary Material

The Supplementary Material is organized as follows. Section 6 describes how the training and test sets are constructed and details the generative models we use. Section 7 details the training and evaluation pipelines for our model and all baselines. Section 12 shows example visualizations from the various datasets used to evaluate DIRE and DID.

6. More Details of Data

6.1. Training Data

We train models separately on each training sets for all baseline methods and our method. Our training data includes the following three training sets: **ImageNet & ablated diffusion model**, **LAION & Kandinsky 3**, and **LAION & Stable Diffusion XL**.

- **ImageNet & ablated diffusion model.** This training set contains 40k real images from the 1k classes of ImageNet [24] and 40k fake images generated by an ablated diffusion model [25] constructed and released by the authors of DIRE [80]. We access the data through the official repository at [this link](#).
- **LAION & Kandinsky 3.** This training set consists of 10k real images randomly sampled from LAION [68] and 10k fake images generated with Kandinsky 3 [2] using prompts randomly drawn from the [Midjourney](#) prompt set. The detailed generation process is described in Section 6.2.
- **LAION & Stable Diffusion XL.** This training set likewise consists of 10k real images randomly sampled from LAION [68] and 10k fake images generated with Stable Diffusion XL (SDXL) [62], using the same pool of [Midjourney](#) prompts. The detailed generation process is described in Section 6.2.

6.2. Evaluation Data

Our evaluation includes both in-distribution and out-of-distribution datasets. For each dataset, the real images are combined with fake images from different sources.

Real images. For each evaluation set, the real images are drawn respectively from three sources: 5k images from [24], 1k images from LAION [68], and 1k images from LSUN-B [91].

Fake images. In ImageNet and LSUN-B based eval-

uation sets, we directly use all the test samples that the DIRE [80] authors provide in the official datasets at [this link](#). In the LAION-based evaluation sets, we considered a more challenging setting. We first randomly sample 1k prompts from [Midjourney](#) and then generate images using several state-of-the-art text-to-image models on Hugging Face.

- **Kandinsky 3.** For Kandinsky 3 images, we use the Kandinsky 3 model [2] from Hugging Face ([kandinsky-community/kandinsky-3](#)), with the default generation parameters.
- **Stable Diffusion XL.** For SDXL images, we follow the standard two-stage Stable Diffusion XL pipeline [62] from Hugging Face: we first generate an initial image with the base model ([stabilityai/stable-diffusion-xl-base-1.0](#)) and then refine it with the refiner model ([stabilityai/stable-diffusion-xl-refiner-1.0](#)), while keeping all other parameters at their default values.
- **Segmind Vega.** For Segmind Vega images, we use the Segmind Vega model [32] from Hugging Face ([segmind/Segmind-Vega](#)), again with the default generation parameters.
- **Playground v2.5.** For Playground v2.5 images, we use the Playground v2.5 model [42] from Hugging Face ([playgroundai/playground-v2.5-1024px-aesthetic](#)), with the default parameters in their usage example.
- **Stable Cascade.** For Stable Cascade images, we follow the official two-stage Stable Cascade [61] setup from Hugging Face: we first sample image latents using the StableCascadePriorPipeline ([stabilityai/stable-cascade-prior](#)), and then decode these latents into RGB images using the StableCascadeDecoderPipeline ([stabilityai/stable-cascade](#)), keeping all other parameters at their default values.

6.3. Validation Data

The validation set follows the same construction pattern as the training data and contains 2k samples from **LAION & Kandinsky 3**, 2k from **LAION & Stable Diffusion XL**, and 10k from **ImageNet & the ablated diffusion model**, respectively, for each training. It is used solely for early stopping to select the best checkpoint. As several baselines

are originally implemented with different early stopping strategies in their public codebases, we retain their strategy primarily to guarantee that the baseline models reach their best performance, and we apply the same protocol as DIRE [80] to our method for a strictly fair comparison on the test sets.

7. More Details of Experiment Implementation

7.1. Reconstruction Module

This section provides implementation details of the reconstruction module used in the Δ and Δ' branches. The reconstruction operator itself follows the standard inversion–reconstruction pipeline described in the main paper (Section 3). Here, we focus solely on the practical settings required for reproducibility, rather than repeating the theoretical formulation.

Inversion and First Reconstruction Each input image is resized or cropped to 256×256 and normalized according to the pretrained diffusion model. We apply deterministic DDIM inversion to obtain the corresponding latent noise representation. During reconstruction, we use DDIM sampling with **20 steps** (`timestep_respacing="ddim20"`) and a fixed $\eta = 0$. A single sampling pass produces the first reconstructed image x'_0 , from which we compute the element-wise absolute reconstruction error $\Delta = |x_0 - x'_0|$.

Second Reconstruction and DiffRecon Features Using x'_0 as the new input, we apply the same DDIM-20 inversion–reconstruction procedure to obtain a second reconstructed image x''_0 . The second-order reconstruction error is defined as $\Delta' = |x'_0 - x''_0|$. We then compute the *DiffRecon* feature as $\Delta^2 = \Delta - \Delta'$. The resulting error maps are mapped to the standard 8-bit intensity range $[0, 255]$ and saved as images, which are subsequently used as inputs to the downstream classifier.

Fixed Inference Without Parameter Updates The reconstruction module operates strictly in inference mode, and all U-Net and diffusion-scheduler parameters remain frozen. We use publicly released ADM checkpoints and adopt a fixed DDIM-20 configuration ($\eta = 0$). Except for the image resolution and sampling settings, the reconstruction module introduces **no additional hyperparameters**.

Dataset-Specific ADM Checkpoints All reconstructions are performed with fixed, publicly released ADM checkpoints. LSUN real and fake images are processed using the ADM model trained on LSUN. All ImageNet and LAION images—including their synthetic variants—are reconstructed using the unconditional ImageNet 256×256

ADM model. No fine-tuning or parameter adaptation is applied; only the appropriate dataset-specific checkpoint is selected, while all other inversion and sampling configurations remain unchanged.

7.2. Training Details

DID (Δ, Δ^2) The two branches of DID are trained independently using the Δ and Δ^2 features generated offline by the reconstruction module. During training, no gradients are back-propagated through the reconstruction process or the diffusion model; only the classifier parameters are updated.

We adopt a ResNet-50 classifier initialized with ImageNet-pretrained weights. All input images are first resized to 256×256 . During training, we apply light augmentation consisting of random cropping to 224×224 and random horizontal flipping, while validation and testing use a center crop to 224×224 . All inputs are normalized.

The classifier is optimized using Adam (default parameters $\beta_1 = 0.9, \beta_2 = 0.999$) with an initial learning rate of 10^{-4} . Binary cross-entropy is used as the loss function. A unified batch size of 256 is used for all methods. Training runs for up to 100 epochs with early stopping based on validation accuracy, and the best validation checkpoint is used for all reported results.

DIRE DIRE is trained in the same way as DID, using the Δ feature as input and following identical preprocessing and classifier settings in their [official repository](#).

LaRE² We reproduce LaRE² using the [official implementation](#) released by the authors and employ the provided `CLIPClassifierWMapV6` as the classifier. The model uses CLIP RN50 as the visual backbone with official pretrained weights.

Before being fed into the network, input images are normalized and padded–center-cropped to 224×224 . Random cropping is applied during training, while validation and testing use a center crop. The classifier is optimized with Adam ($\beta_1 = 0.9, \beta_2 = 0.999$) using a learning rate of 10^{-4} and a batch size of 256. The learning rate is adaptively reduced using `ReduceLROnPlateau` based on validation accuracy, with a minimum learning rate of 10^{-7} .

AEROBLADE (AERO.) AEROBLADE is used as a training–free baseline. The [official implementation](#) computes reconstruction errors with the pretrained diffusion autoencoder and evaluates them using ROC–based metrics such as AUC, without introducing any learning or threshold selection. We follow this setting and keep the autoencoder fixed throughout.

For consistent evaluation across all methods, we introduce a lightweight calibration step: reconstruction scores

Table 5. Accuracy (%) of DID trained on the PNG-only variant. Left block: trained on **LAION & Kan.3**. Right block: trained on **LAION & SDXL**. Models are evaluated on PNG, JPEG 95, and JPEG 75 versions of each test set. All averages are computed from raw values and then rounded to two decimals.

Gen. model	LAION & Kan.3 (PNG-only training)			LAION & SDXL		
	PNG	JPG95	JPG75	PNG	JPG95	JPG75
Kan.3	97.2	98.9	95.1	90.6	85.4	70.4
SDXL	93.2	88.9	76.3	97.3	97.1	85.6
Vega	89.1	84.3	72.3	95.2	93.0	76.3
Playground v2.5	94.9	92.9	82.7	91.6	88.0	73.4
Stable Cascade	96.2	95.6	89.4	94.4	87.2	71.7
Avg.	94.09	92.09	83.15	93.81	90.13	75.46

are computed on the training split and a fixed operating threshold is chosen as the 95th percentile of the training scores. This threshold is applied to the test split to compute the reported ACC. No parameter optimization is involved, and AEROBLADE remains fully training-free.

UniversalFakeDetect (UFD) UniversalFakeDetect is used as a supervised baseline. Following the [official implementation](#) and released configuration, we use a pretrained CLIP ViT-L/14 backbone together with a linear binary classifier for distinguishing real and generated images. The backbone is kept frozen during training, and only the classification head is updated on the training split.

All images are resized to 256×256 , cropped to 224×224 , augmented with random cropping and horizontal flipping during training, and normalized. The classifier head is trained with BCE-with-logits loss using the AdamW optimizer ($\beta_1 = 0.9, \beta_2 = 0.999$), a batch size of 256, and an initial learning rate of 10^{-4} . Validation accuracy is used for model selection, and the best checkpoint is reported on the test split.

8. Sensitivity to image formats.

In the main experiments, real images are provided in JPEG format while generated images are stored as PNG files, following the original DIRE setup. To verify that DID does not rely on such JPEG/PNG container differences, we conduct an additional sensitivity analysis.

We rebuild the training set so that all real images come from their official PNG releases (the fake images are already PNG), making the entire training set natively PNG. We then train DID on this PNG-only data and evaluate the resulting model on three test variants: native PNG, JPEG 95, and JPEG 75, all derived from the same PNG originals.

As shown in Table 5, DID maintains consistently high performance across all formats. This demonstrates that DID does not depend on JPEG/PNG encoding artifacts and in-

stead captures intrinsic differences between real and generated images.

9. New baselines and datasets

We further compare DID with two newly added baselines, *Effort* [85] and *DDA* [18], under two training setups: training all models on (i) *GenImage* [101] (Table 6) and (ii) *ImageNet* (Table 7). We then evaluate these models on *GenImage* [101], *GenDet* [100], and our two original test datasets, *LAION* and *ImageNet*. In addition to the original ACC metric, we also report two newly added metrics, ROC-AUC and FPR@TPR95. Across both tables, DID consistently outperforms all baselines.

10. Computation and Memory Cost

Table 8 reports the inference cost on a single NVIDIA A800 GPU. DID takes 2.46 seconds per image, including both reconstruction and testing. For comparison, DIRE and LaRE take 1.35s and 0.75s per image, respectively. Although DID is slower, it provides a clear accuracy gain (Table 1 in the main text). DID’s peak GPU memory is similar to DIRE (Table 8), so it can run on a single GPU.

11. Ablation on Fusion Strategy

Our method uses two separate classifiers to process 1st- and 2nd-order signals, and combines their outputs with an additive gate. This section studies the fusion strategy. Specifically, we compare our score-level fusion (two classifiers with an additive gate) with a feature-level variant that concatenates 1st- and 2nd-order features and feeds them into a single classifier.

As shown in Table 9, the single-classifier variant achieves performance comparable to our main design. We keep the two-classifier design mainly for simplicity and interpretability. Since 1st- and 2nd-order reconstruction errors capture different signals, separating them makes the

Table 6. Acc (%) / AUROC / FPR@TPR95 (%) of DID (with two thresholds) and two additional baselines (*Effort* and *DDA*). All detectors are trained on *GenImage* and evaluated on *GenImage*, *GenDet*, and our two original test datasets. To avoid excessive 1.00 values, we report AUROC with three decimal places.

Eval set	Gen. model	DID _{0.29}	DID _{0.5}	Effort	DDA
GenImage	ADM	<u>99.90/1.000/0.00</u>	100.00/1.000/0.00	98.55/0.999/0.40	99.30/ 1.000/0.20
	BigGAN	<u>99.90/1.000/0.00</u>	99.95/1.000/0.00	95.45/0.995/2.60	98.70/0.999/0.50
	GLIDE	<u>99.90/1.000/0.00</u>	100.00/1.000/0.00	98.35/0.999/0.20	99.20/ 1.000/0.20
	Midjourney	99.70/1.000/0.00	99.70/1.000/0.00	<u>57.25/0.744/80.00</u>	54.95/ <u>0.845/56.30</u>
	SD-v1.4	<u>99.45/1.000/0.00</u>	99.50/1.000/0.00	86.70/ <u>0.975/13.00</u>	72.81/0.965/15.60
	SD-v1.5	99.50/1.000/0.00	<u>99.40/1.000/0.00</u>	83.95/ <u>0.975/11.30</u>	72.65/0.962/16.50
	VQDM	99.90/1.000/0.00	99.90/1.000/0.00	97.00/ <u>0.997/1.80</u>	<u>99.50/1.000/0.30</u>
	Wukong	99.20/1.000/0.00	<u>99.15/1.000/0.00</u>	83.05/ <u>0.969/15.60</u>	74.50/0.968/ <u>11.00</u>
	Avg.	<u>99.68/1.000/0.00</u>	99.70/1.000/0.00	87.54/0.957/15.61	83.95/ <u>0.967/12.33</u>
GenDet	BigGAN	99.95/1.000/0.00	99.95/1.000/0.00	98.55/ 1.000/0.10	<u>99.20/1.000/0.00</u>
	CRN	99.95/1.000/0.00	99.95/1.000/0.00	98.15/0.998/0.60	<u>98.45/0.999/0.40</u>
	DeepFake	99.65/1.000/0.00	<u>99.45/1.000/0.00</u>	96.35/0.995/2.50	99.20/1.000/0.00
	GauGAN	99.95/1.000/0.00	99.95/1.000/0.00	97.45/0.997/0.90	99.35/1.000/0.00
	IMLE	99.95/1.000/0.00	99.95/1.000/0.00	<u>98.70/1.000/0.10</u>	<u>97.70/0.998/1.00</u>
	StarGAN	99.95/1.000/0.00	99.95/1.000/0.00	<u>98.50/0.999/0.20</u>	99.35/1.000/0.00
	Avg.	99.90/1.000/0.00	<u>99.87/1.000/0.00</u>	97.95/0.998/0.73	98.88/ <u>0.999/0.23</u>
LAION	Kan.3	99.60/1.000/0.00	99.60/1.000/0.00	63.85/0.845/61.00	57.10/0.832/48.20
	SDXL	99.60/0.999/0.00	<u>99.50/0.999/0.00</u>	66.85/0.870/59.20	67.70/0.907/31.50
	Vega	98.90/0.999/0.00	<u>98.75/0.999/0.00</u>	57.50/0.753/78.10	76.90/ <u>0.943/23.30</u>
	Playground v2.5	99.60/1.000/0.00	<u>99.55/1.000/0.00</u>	67.05/0.865/62.70	81.55/ <u>0.959/17.70</u>
	Stable Cascade	99.65/1.000/0.00	<u>99.55/1.000/0.00</u>	81.20/ <u>0.960/20.00</u>	69.20/0.920/28.00
	Avg.	99.47/0.999/0.00	<u>99.39/0.999/0.00</u>	67.29/0.859/56.20	70.49/ <u>0.912/29.74</u>
ImageNet	ADM	99.65/1.000/0.00	99.65/1.000/0.00	97.20/0.996/1.20	<u>99.05/1.000/0.20</u>
	SDv1	99.35/1.000/0.00	<u>98.70/1.000/0.00</u>	84.70/0.963/18.10	71.05/0.967/12.10
		Avg.	99.50/1.000/0.00	<u>99.17/1.000/0.00</u>	90.95/0.979/9.65
Total average		99.68/1.000/0.00	<u>99.62/1.000/0.00</u>	86.02/0.947/20.46	85.11/ <u>0.965/12.43</u>

contribution of each signal easier to analyze. The two-classifier design is also more memory-efficient, as it uses fewer parameters than the single-classifier variant.

12. More Visualization About DID

In this section, we provide additional visualizations to illustrate how DID behaves across real images and a wide range of generative models. Figure 4 summarizes the key differences between first-order and second-order residuals, while Figures 5–11 present more detailed residual matrices for each model. Together, these visualizations highlight the limitations of first-order residuals and the improved consistency achieved by our second-order module.

Table 7. Acc (%) / AUROC / FPR@TPR95 (%) of DID (with two thresholds) and two additional baselines (*Effort* and *DDA*). All detectors are trained on *ImageNet* and evaluated on *GenImage*, *GenDet*, and our two original test datasets, *LAION* and *ImageNet*. To avoid excessive 1.00 values, we report AUROC with three decimal places.

Eval set	Gen. model	DID _{0.29}	DID _{0.5}	Effort	DDA
GenImage	ADM	<u>99.20/1.000/0.00</u>	99.50/1.000/0.00	86.30/0.986/6.70	98.30/0.999/0.10
	BigGAN	<u>99.10/1.000/0.00</u>	99.40/1.000/0.00	80.15/0.878/39.00	98.50/1.000/0.00
	GLIDE	<u>99.20/1.000/0.00</u>	99.50/1.000/0.00	85.85/0.973/12.80	97.50/0.998/0.90
	Midjourney	<u>99.20/1.000/0.00</u>	99.50/1.000/0.00	57.00/0.597/90.20	56.15/0.810/58.80
	SD-v1.4	<u>99.20/1.000/0.00</u>	99.50/1.000/0.00	85.30/0.958/19.10	82.91/0.969/13.30
	SD-v1.5	<u>99.20/1.000/0.00</u>	99.50/1.000/0.00	84.75/0.950/22.10	83.60/0.967/17.00
	VQDM	<u>99.20/1.000/0.00</u>	99.50/1.000/0.00	86.45/0.991/5.40	98.55/1.000/0.00
	Wukong	<u>99.20/1.000/0.00</u>	99.45/1.000/0.00	84.40/0.949/22.80	84.10/0.973/12.70
	Avg.	<u>99.19/1.000/0.00</u>	99.48/1.000/0.00	81.28/0.910/27.26	87.45/0.964/12.85
GenDet	BigGAN	<u>99.85/1.000/0.00</u>	99.90/1.000/0.00	99.70/1.000/0.00	99.45/1.000/0.00
	CRN	<u>99.85/1.000/0.00</u>	99.90/1.000/0.00	98.80/1.000/0.30	99.35/0.999/0.10
	DeepFake	99.50/1.000/0.10	99.20/1.000/0.10	96.75/0.997/0.80	99.30/1.000/0.00
	GauGAN	<u>99.85/1.000/0.00</u>	99.90/1.000/0.00	99.65/1.000/0.00	99.60/1.000/0.00
	IMLE	<u>99.85/1.000/0.00</u>	99.90/1.000/0.00	99.75/1.000/0.00	99.40/1.000/0.10
	StarGAN	<u>99.85/1.000/0.00</u>	99.90/1.000/0.00	99.65/1.000/0.00	99.60/1.000/0.00
		Avg.	99.79/1.000/0.02	<u>99.78/1.000/0.02</u>	99.05/0.999/0.18
LAION	Kan.3	<u>99.30/1.000/0.00</u>	99.55/1.000/0.00	80.75/0.934/31.30	59.05/0.826/47.70
	Playground v2.5	<u>99.30/1.000/0.00</u>	99.60/1.000/0.00	83.95/0.941/28.60	87.00/0.962/14.80
	SDXL	<u>99.25/0.999/0.00</u>	99.55/0.999/0.00	85.00/0.953/21.30	76.30/0.911/35.20
	Stable Cascade	<u>99.35/1.000/0.00</u>	99.65/1.000/0.00	90.60/0.976/12.60	75.50/0.928/25.40
	Vega	<u>99.25/1.000/0.00</u>	99.55/1.000/0.00	79.85/0.922/34.30	80.80/0.944/22.30
		Avg.	<u>99.29/1.000/0.00</u>	99.58/1.000/0.00	84.03/0.945/25.62
ImageNet	ADM	<u>99.85/1.000/0.00</u>	99.90/1.000/0.00	99.40/0.999/0.00	99.55/1.000/0.00
	SDv1	<u>99.85/1.000/0.00</u>	99.90/1.000/0.00	98.10/0.999/0.30	83.45/0.987/6.40
		Avg.	<u>99.85/1.000/0.00</u>	99.90/1.000/0.00	98.75/1.000/0.15
Total average		<u>99.45/1.000/0.00</u>	99.63/1.000/0.00	88.67/0.953/16.55	88.47/0.965/12.13

Table 8. Per-image inference time (seconds) and memory usage (MB) for LaRE2, DIRE, and DID.

Method	Reconstruction Time (Memory)	Testing Time (Memory)
LaRE2	0.09 (33.34)	0.66 (9.74)
DIRE	1.01 (396.48)	0.34 (21.77)
DID	2.01 (398.39)	0.45 (22.55)

Table 9. Acc(%) / AUROC / FPR@TPR95(%) of DID_{0.29} and a variant that fits both 1st- and 2nd-order signals into a single classifier (DID_{SC}).

Train set	Eval set	LAION	ImageNet
ImageNet	DID _{0.29}	99.29/1.00/0.00	99.85/1.00/0.00
	DID _{SC}	99.03/1.00/0.00	99.45/1.00/0.00

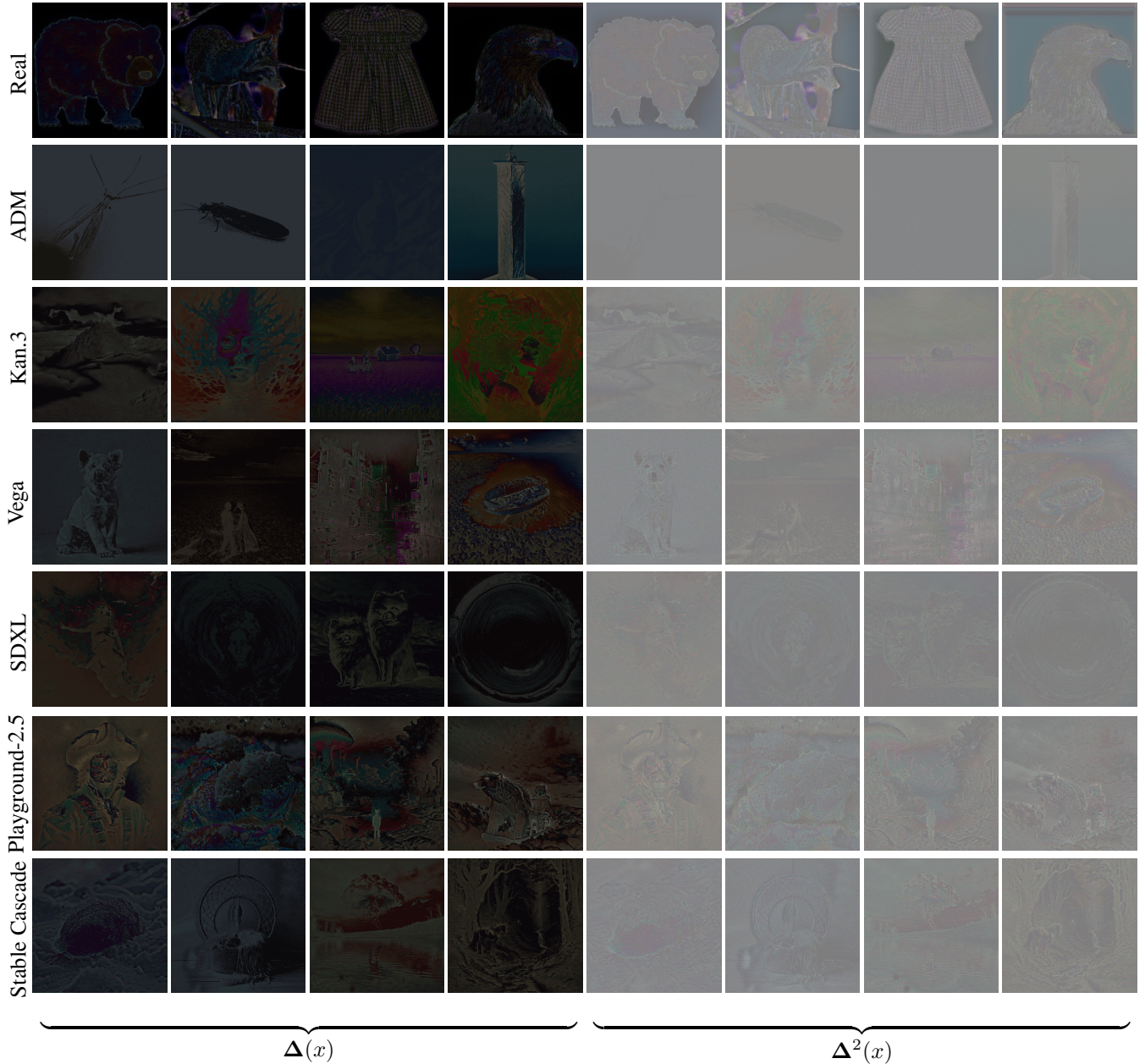


Figure 4. **Comparison of first-order and second-order residuals across real and generated images.** The DIRE framework [80] shows that real images typically produce sharper and more structured first-order residuals Δx , whereas fake images tend to yield weaker patterns. However, in broader evaluation across diverse and strong generative models, first-order residuals are not always stable when the real and synthetic distributions are close. In more challenging cases, fake images can even produce stronger residual signals than real images, leading to potential misclassification. In contrast, our proposed second-order residual module $\Delta^2 x$ provides more consistent separability between real and fake samples by taking the difference between the reconstruction error of the input image and that of its reconstructed version.



Figure 5. **Visualization of real images across the DID pipeline.** We show the original image x , the first reconstruction x' , the second reconstruction x'' , and their corresponding residual maps Δx , $\Delta x'$, and $\Delta^2 x$.

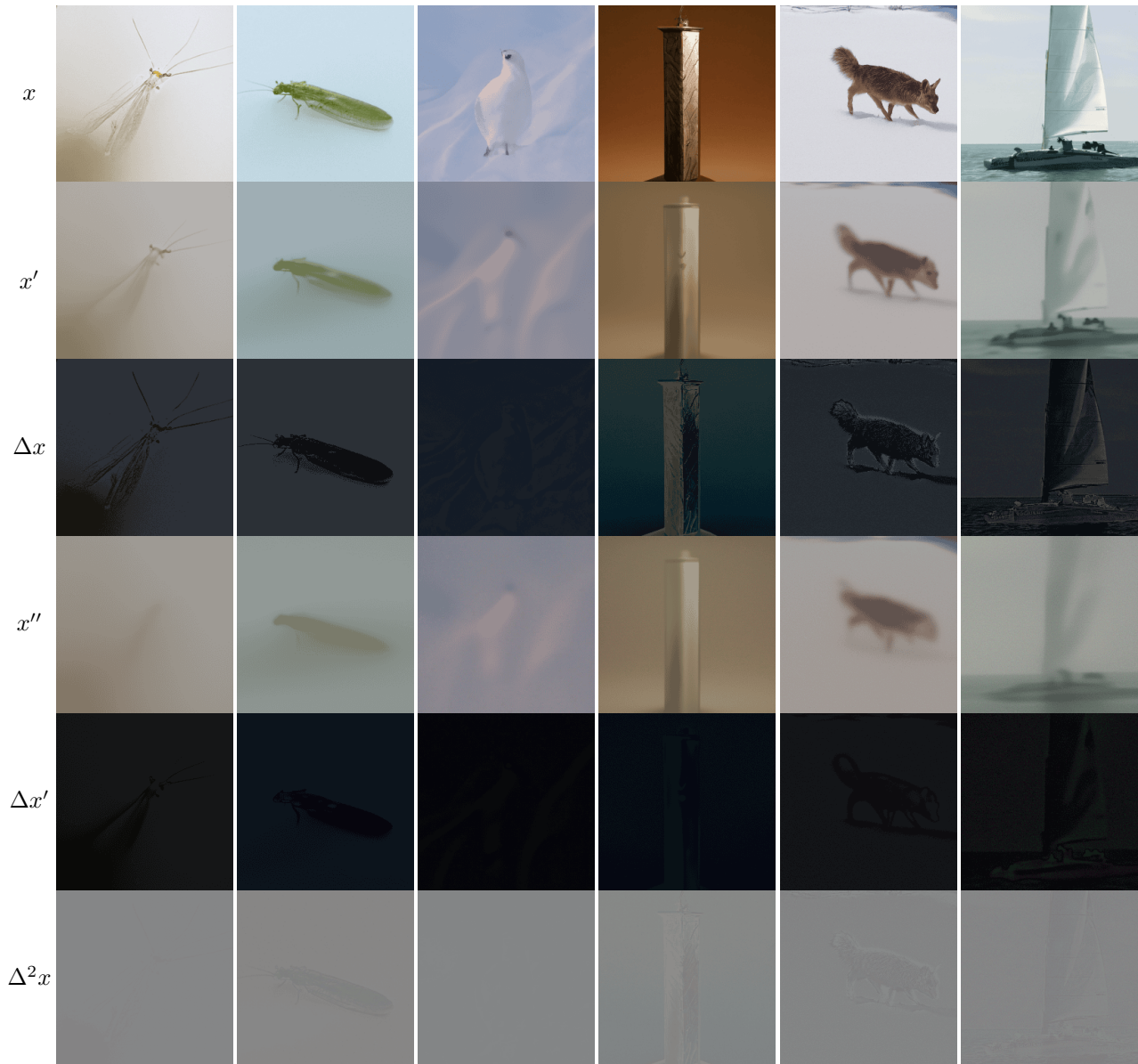


Figure 6. **Visualization of ADM-generated fake images from the ImageNet subset constructed in the DIRE dataset.** For each ImageNet class (“A photo of class”, class from ImageNet [24]), we show the ADM-generated image x , its first reconstruction x' , the second reconstruction x'' , and their corresponding residual maps Δx , $\Delta x'$, and $\Delta^2 x$.



Figure 7. **Visualization of Kan3-generated images constructed for our dataset.** For each sample, we show the original synthesized image x , the first reconstruction x' , the second reconstruction x'' , and their corresponding residual maps Δx , $\Delta x'$, and $\Delta^2 x$. All Kan3 images are generated using prompts collected from Midjourney.

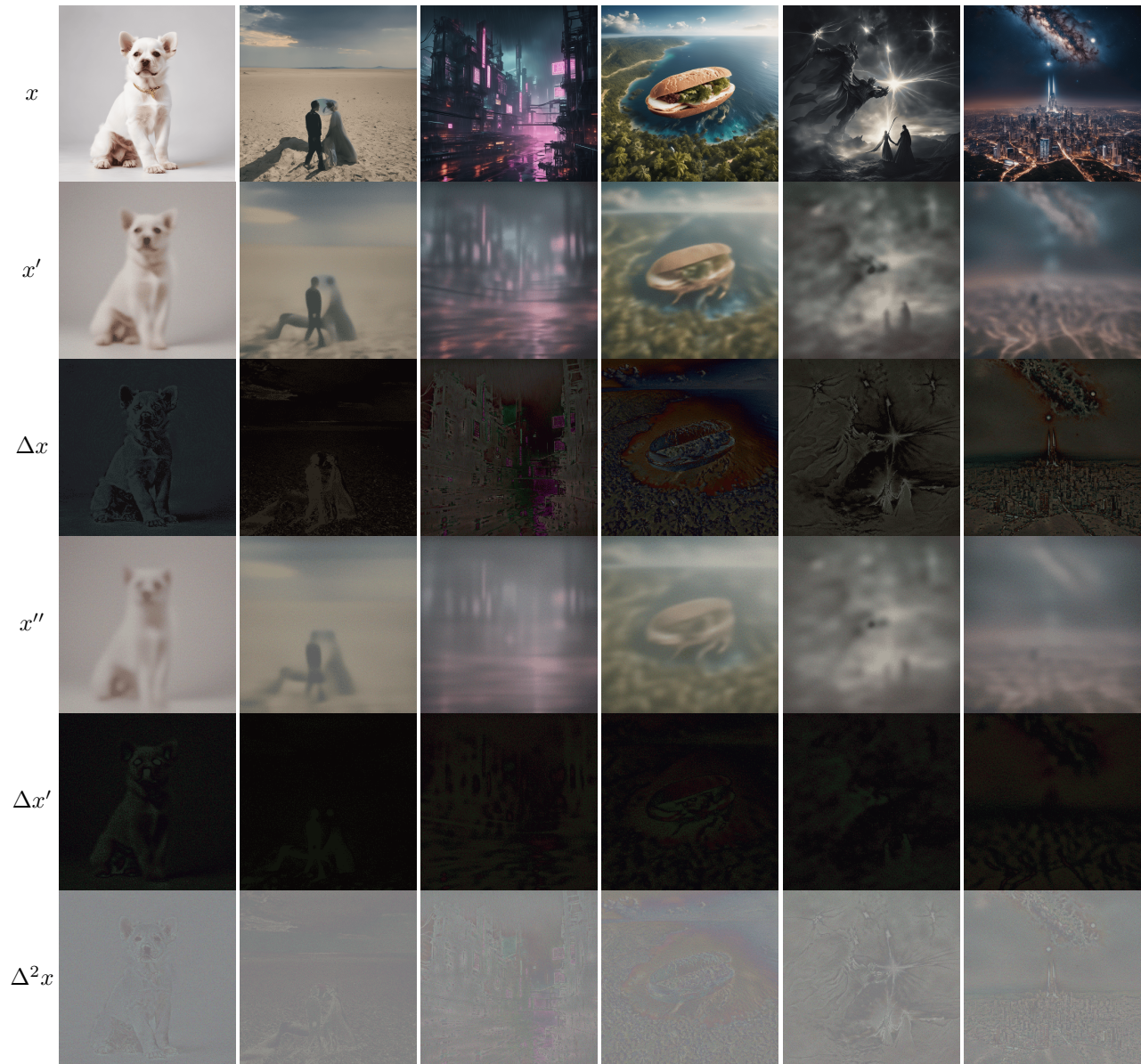


Figure 8. **Visualization of Vega-generated images constructed for our dataset.** For each sample, we show the original synthesized image x , the first reconstruction x' , the second reconstruction x'' , and their corresponding residual maps Δx , $\Delta x'$, and $\Delta^2 x$. All Vega images are generated using prompts collected from Midjourney.

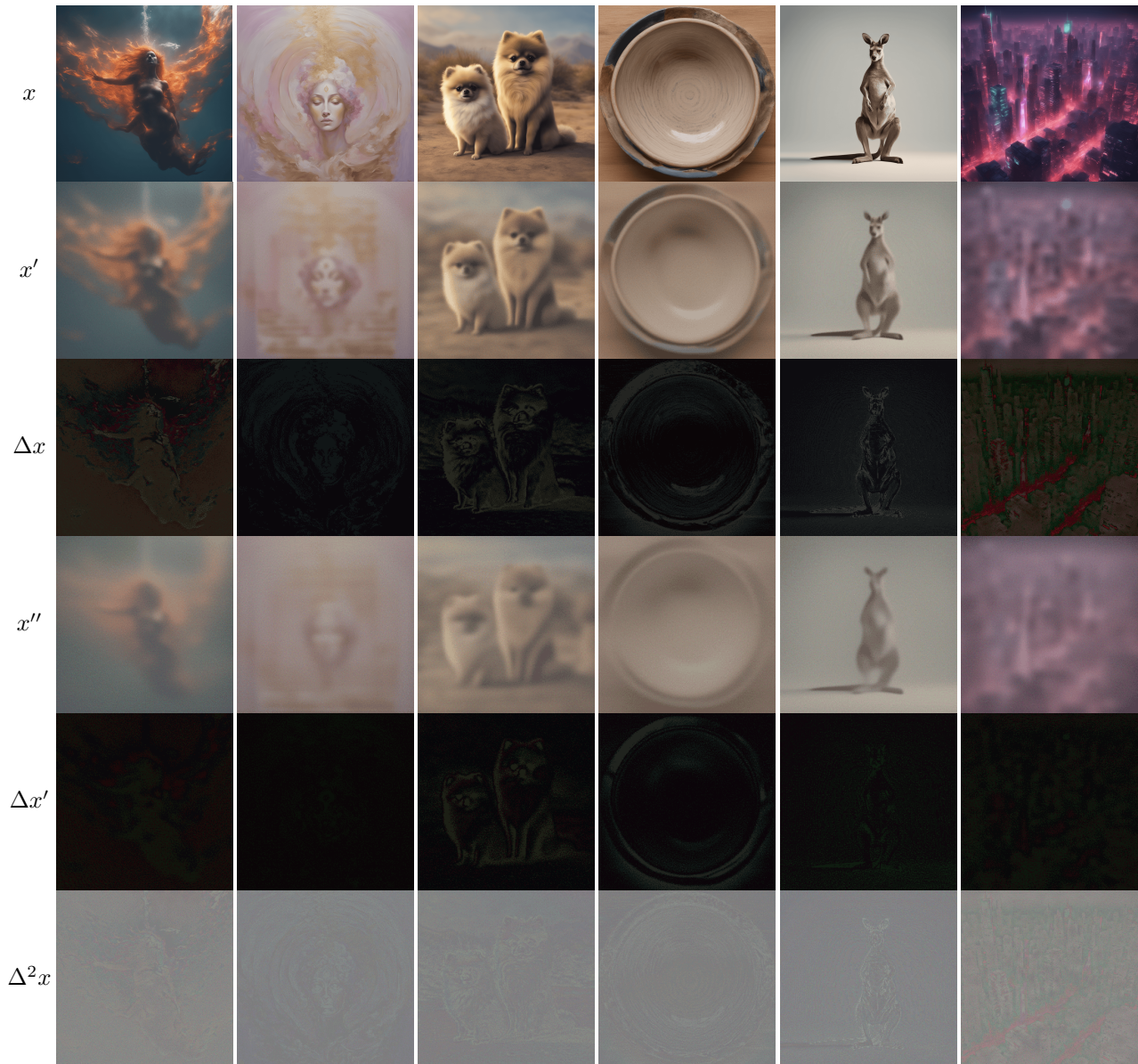


Figure 9. **Visualization of SDXL-generated images constructed for our dataset.** For each sample, we show the original synthesized image x , the first reconstruction x' , the second reconstruction x'' , and their corresponding residual maps Δx , $\Delta x'$, and $\Delta^2 x$. All SDXL images are generated using prompts collected from Midjourney.

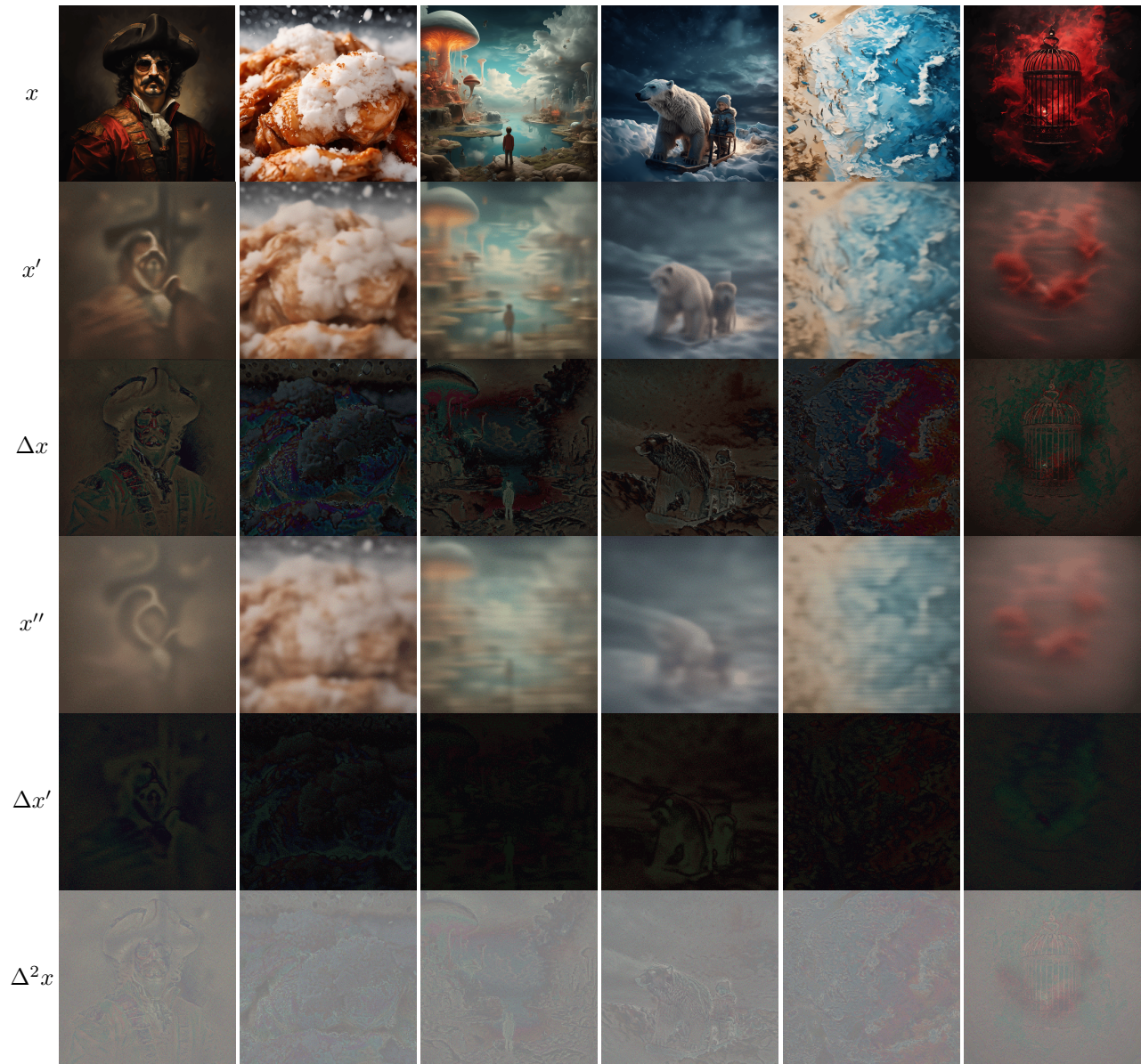


Figure 10. **Visualization of playground-2.5-generated images constructed for our dataset.** For each sample, we show the original synthesized image x , the first reconstruction x' , the second reconstruction x'' , and their corresponding residual maps Δx , $\Delta x'$, and $\Delta^2 x$. All playground-2.5 images are generated using prompts collected from Midjourney.



Figure 11. **Visualization of Stable Cascade-generated images constructed for our dataset.** For each sample, we show the original synthesized image x , the first reconstruction x' , the second reconstruction x'' , and their corresponding residual maps Δx , $\Delta x'$, and $\Delta^2 x$. All Stable Cascade images are generated using prompts collected from Midjourney.